Manuscript 9054 - Revision 1

Electrical Properties of Iron Sulfide-bearing Dunite under Pressure: Effect of Temperature, Composition, and Annealing Time

Michael J. Tauber[1,2,3*], Suryansh Saxena[2], Emma S. Bullock[3], Hélène Ginestet[3,4], Anne Pommier[2,3*]

[1] UC San Diego, Department of Chemistry and Biochemistry, La Jolla, CA 92093, USA

[2] UC San Diego, Materials Science and Engineering Program, La Jolla, CA 92093, USA

[3] Carnegie Institution for Science, Earth and Planets Laboratory, Washington, DC 20015, USA

[4] University of Lille, Department of Physics, 59655 Villeneuve d'Ascq, France

* Corresponding authors: apommier@carnegiescience.edu; mtauber@ucsd.edu

This is the peer-reviewed, final accepted version for American Mineralogist, published by the Mineralogical Society of America.
The published version is subject to change. Cite as Authors (Year) Title. American Mineralogist, in press.
DOI: https://doi.org/10.2138/am-2023-9054. http://www.minsocam.org/

ABSTRACT

The detection and quantification of metal sulfides in host rocks by electrical measurements have been priorities for field and laboratory studies, motivated by mineral prospecting, fundamental interest in the mantle structure or core/mantle differentiation, among other reasons. Here, we reanalyze electrical data for a dunite host with added FeS or Fe-S-Ni (Saxena et al., 2021), and report additional experimental runs along with electron microprobe analyses. The applied pressure was 2 GPa; impedance spectra were acquired while annealing at 1023 K (below the metal-sulfide solidus), and while varying temperature from 570 to 1650 K. Addition of 6.5- or 18-vol.% FeS strongly enhances conductivity of the bulk sample compared with that of the dunite host, though values are 100 – 100,000 times less than those of pure FeS. These results indicate that most metal sulfide content is not part of a viable conductive path, even for the 18-vol.% quantity. Nevertheless, the relatively high conductivity and weak temperature dependence of the 18-vol.% sample reveal that contiguous paths of solid or molten FeS span the electrodes. The sample with 6.5-vol.% sulfide also exceeds the percolation threshold for temperatures as low as ~100 K below the eutectic melting point, likely because FeS softens. Conductivity is nearly unchanged upon crossing the eutectic temperature, however a decline over 1400 – 1500 K reveals that the 6.5 vol.% molten FeS forms a fragile electrical network in dunite. Samples with $Fe_{50}S_{40}Ni_{10}$ or $Fe_{40}S_{40}Ni_{20}$ (at.%) are less conductive than pure dunite at temperatures below ~1450 K. This surprising result, likely caused by a reducing influence of Fe or Ni metal, does not support the use of FeS as an analog for compositions with nickel or excess metal. Our findings suggest that probing the electrical network of metal sulfides as solids complements other studies focused on connectivity of molten metal sulfides.

Keywords: impedance spectroscopy, electrical conductivity, metal sulfide, xenolith, percolation threshold

INTRODUCTION

The study of metal sulfide networks in host rocks relates to numerous aspects of earth and planetary science, ranging from planetary differentiation (Minarik, 2003; Yoshino et al., 2003, 2004; Terasaki et al., 2005, 2008; Bagdassarov et al., 2009a,b; Watson and Roberts, 2011; Walte et al., 2011; Solferino et al., 2020), to high-conductivity anomalies in cratonic environments (Evans et al., 2011; Saxena et al., 2021 and references therein), to economic geology (Fontboté et al., 2017; Barnes et al., 2017). A longstanding challenge in the field has been to correlate the type and quantity of metal sulfide in host rocks, with electrical properties (e.g., Rogers, 1966; Revil et al., 2022; Zhdanov et al., 2018). Given great differences in resistivity between metal sulfides and typical silicate hosts, the distribution of the conductive phase (e.g., as isolated grains vs. dendrites) has a strong impact on the electrical properties (Parkhomenko, 1967). Additionally, the sulfides themselves can span a large range of conductivity values, even for minerals of the same classification (Parkhomenko, 1967; Pearce et al., 2006). Despite these sources of complexity, various reports have presented correlations between sulfide content and conductivity, and certain threshold quantities have been highlighted. For example, Anderson (1960), in a relatively early report of a field study, described that sulfide minerals in excess of 5 wt.% formed a connected network within a peridotite host, thereby dramatically decreasing bulk resistivity. Parkhomenko (1967) highlighted that 3 – 10 wt.% Cu, Ni-bearing sulfides, or 5% pyrrhotite, made certain rocks highly conductive. Similarly, 7 wt.% was identified by Nelson and Van Voorhis (1983) as a threshold for the largest change in

resistivity, based on induced polarization measurements of sulfides in a variety of rock types. The reason for similar threshold values in the preceding examples is unclear.

In laboratory studies of metal sulfides in a silicate matrix, Yoshino et al. (2003, 2004) reported the first electrical measurements under pressure (1 or 3 GPa) and as a function of temperature. Upon heating samples of olivine or peridotite with 3 – 13 vol.% FeS or $Fe_{64}S_{36}$ (at.%), electrical conductivities much greater than those of the host were recorded for samples with iron sulfide concentrations ≥ 6 vol.%. The elevated conductivity levels persisted over annealing periods as long as 3 days, at temperatures for which the sulfides were fully melted. These measurements were interpreted as support for a percolation threshold of 6 vol.% sulfide. By contrast, Bagdassarov et al. (2009a) presented electrical measurements at 1 GPa pressure that supported substantially higher percolation thresholds, namely ~17.5 vol.% for $Fe_{57}S_{43}$ (at.%) in olivine, and >15 vol.% (lower bound) in peridotite. These thresholds were based upon experiments which included annealing at temperatures just below the Fe-FeS eutectic melting point for periods as long as 5 days. When temperatures were increased slightly above the eutectic point, conductivity values that were initially high for all samples were found to drop sharply, except for 20 vol.% iron sulfide in olivine. Subsequently, Watson et al. (2010) and Watson and Roberts (2011) explored lower concentrations (1 to 10 vol.%) of $Fe_{54}S_{46}$ in olivine, and reported significantly better conductivity for 1 vol.% iron sulfide relative to the host, and much greater increases for samples with 4 or more vol.%. Based on the unusual and powerful combination of electrical characterization with X-ray tomography, the 2011 study also provided some additional general insights, e.g., the sensitivity of conductivity measurements for detecting the onset of connectivity (Watson and Roberts, 2011).

Some of the variation in electrical results for the laboratory studies could be attributed to

differences in grain sizes of the olivine or peridotite host, or differences in annealing temperatures and times, as well as subsequent heating conditions. However, the reasons for differing percolation thresholds is still unsettled. Additionally, the factors that cause some experiments to have highly conductive networks in the solid state (Bagdassarov et al., 2009a), apparently without prior heating above the eutectic temperature, are uncertain. Questions also remain regarding the effect on bulk conductivity caused by adding common alloying elements such as Cu or Ni to the sulfide portion. In general, further laboratory studies at elevated pressures and temperatures are needed to reach a better understanding of the electrical properties of sulfide-bearing rocks, so that conductivity models can be developed and applied to the field.

Here, we reanalyze our previously reported electrical data (Saxena et al., 2021) for experiments involving metal sulfide in a dunite host, and present additional electrical experiments that explore the effect of metal sulfide chemistry (Fe-S-Ni). The present report also includes extensive microprobe analyses of the samples, which were unavailable in our previous study. One motivation for considering different sulfides is to reproduce some of the natural compositions and to understand whether, from an electrical standpoint, a silicate-metal sulfide mixture with a simplified chemistry (FeS) can be a useful analog of more complex mixtures. Experiments were performed under a pressure of 2 GPa (equivalent to ~60 km depth in the Earth's upper mantle) and over a large temperature range of 573-1650 K. Our focus was not to address aspects that are central to core-mantle differentiation. Instead, the experimental choices (e.g., relatively low annealing temperature) allow this study to have the most relevance to cratonic settings, and to provide unique insights into the nature of connectivity for both solid and molten metal sulfides in a silicate host.

This is the peer-reviewed, final accepted version for American Mineralogist, published by the Mineralogical Society of America.
The published version is subject to change. Cite as Authors (Year) Title. American Mineralogist, in press.
DOI: https://doi.org/10.2138/am-2023-9054. http://www.minsocam.org/

115

116

117 ## EXPERIMENTAL PROCEDURE AND ANALYSES

118 ### Starting materials and sample preparation

119 Electrical measurements were performed on pure silicate aggregates, metal sulfides, and
120 their mixtures. Experimental conditions are listed in **Table 1**. The starting material for the
121 polycrystalline silicate aggregate is a natural dunite composed of 95 vol.% olivine, 4 vol.%
122 clinopyroxene, and 1 vol.% chromite from Engorora, northern Tanzania (sample ENG-8 as
123 described in Chin, 2018; same as dunite ENG8 in Saxena et al., 2021). The material is
124 pulverized, and based on SEM analysis (Thermo-Fisher Pathfinder) of thousands of particles, the
125 vast majority have cross-sections with an area-equivalent diameter in the range 0.5 to 4 μm. This
126 range corrects our previous assessment of 10 (+/-1) μm (Saxena et al., 2021). The Mg# is 86. In
127 this paper, metal sulfide refers to any of the compositions included in our electrical
128 measurements (**Table 1**), including FeS (=$Fe_{50}S_{50}$), $Fe_{50}S_{40}Ni_{10}$, or $Fe_{40}S_{40}Ni_{20}$ (all written as
129 atom %). These sulfide compositions are analogous to ones reported previously in the upper
130 mantle (e.g., Fleet and Stone, 1990; Guo et al. 1999; Aulbach et al., 2004; Wang et al., 2010;
131 Delpech et al., 2012). The $Fe_{50}S_{40}Ni_{10}$ and $Fe_{40}S_{40}Ni_{20}$ samples were prepared by mixing
132 appropriate quantities of FeS, Fe, and Ni powders (>99% pure, Alfa Aesar; ~10 μm diameter).
133 Next, metal sulfides and dunite powders, with the relative volumetric amounts specified in **Table**
134 **1** (3 or 3.4, 6.5 and 18.2 vol.% metal sulfide), were mixed in acetone using an agate mortar and
135 pestle. After drying, all samples were stored in a desiccator.

136

137 ### Electrical experiments in the multi-anvil press

Electrical experiments were carried out at 2 GPa under quasi-hydrostatic conditions in a Walker-type multi-anvil press (Rockland Research). The pressure was applied using eight tungsten carbide cubes with corner-truncated edge length of 8 mm, and MgO octahedral pressure media with an edge length of 14 mm. The electrical cell assembly was described previously (COMPRES design; Saxena et al., 2021). Briefly, the cell includes an MgO sample sleeve which encloses three stacked alumina rings separated by two high-purity Fe disks. All MgO parts were fired at ≥1273 K and stored in a desiccator until use. The immediate containment of the sample consists of the middle alumina ring and two Fe disks, and the design prevents molten material from escaping at high temperatures. The sample is heated by applying a current to the surrounding Re foil, and temperature is monitored using one of two Type-C thermocouples ($W_{95}Re_5$-$W_{74}Re_{26}$). Each thermocouple contacts one of the Fe-metal disks which serve as electrodes for impedance measurements.

The cell assembly was initially compressed to the target pressure (2 GPa) at room temperature. The pressure remained within (±) 2% of the target value throughout the heating and cooling cycles. **Figure S1** shows the temperature-time paths for each experiment. Power was applied to the furnace to increase the sample temperature in 25 K increments until 1023 K was reached (rise time ~40 minutes). One reason for selecting this annealing temperature is that it lies significantly below the Fe-FeS eutectic temperature (1260 - 1280 K, based on data from 2 – 3 GPa: Brett and Bell, 1969; Ryzhenko and Kennedy, 1973; Usselman, 1975). The eutectic temperature of samples with added nickel could be significantly lower (see Discussion regarding this topic), nevertheless the annealing is well below (100 K or more) any conceivable solidus temperature. This choice allowed the subsequent variable-temperature impedance measurements to probe the electrical characteristics as the metal sulfide melted in the sample for the first time.

By contrast, annealing with a molten metal sulfide would have caused irreversible changes to the sample that we preferred to avoid as a starting point for variable-temperature measurements. After the sample reached 1023 K, impedance spectra were acquired while annealing for 3.5 to 27.4 hours, until a relatively steady resistance value was recorded. Following the annealing stage, all samples except BB303 and BB304 were cooled to a low temperature between 570 and 720 K. The time to reach these low temperatures was 30 – 80 minutes for all samples except BB305, which took ~130 minutes. The cooling rates were –3 to –10 K/min, with average –7 K/min. All samples except BB303, BB304, and BB305 were then heated to a final temperature ranging between 1570 and 1650 K. The heating rates were +3.5 to +9.3 K/min, with average +5 K/min. Impedance spectra were collected at regular temperature intervals throughout cooling and heating cycles. All experiments were quenched by turning off the power to the heater. After a slow decompression, the electrical cell was retrieved and mounted in an epoxy resin. The cell and sample were sliced longitudinally and polished to expose the surface for chemical and textural analyses.

Electrical measurements were made with an impedance spectrometer (Ametek/Solartron 1260 impedance gain/phase analyzer) using the four-electrode technique. A DC potential of 1 V with 100 mV AC amplitude was applied over a range of frequencies to measure the complex impedance. The range of frequencies depended on the nature of the sample. The frequency range varied from 50 Hz to 0.1 Hz for pure metal sulfide samples (and 18.2 vol.% FeS + dunite), and from 5 MHz to 1 Hz for all other samples.

Impedance spectroscopy background and analysis

This is the peer-reviewed, final accepted version for American Mineralogist, published by the Mineralogical Society of America.
The published version is subject to change. Cite as Authors (Year) Title. American Mineralogist, in press.
DOI: https://doi.org/10.2138/am-2023-9054. http://www.minsocam.org/

Impedance (Z^*) is defined as the opposition to the flow of alternating current at a defined frequency. It consists of a real part (resistive component, Z') and an imaginary part (reactive component, Z''). The overall resistance of the bulk sample, alumina ring, and Fe disks is assessed by visual inspection of plots of frequency-dependent values of Z'' vs. Z' (Nyquist plots) based on the intersection, or extrapolated intersection, of the right-most impedance arc at relatively low frequency, with the real axis. For those curves that can be fitted to an equivalent electrical circuit (see representative comparisons in **Figure S2**), the value for Z' resulting from least-squares optimization differs less than 10% from the value based on visual inspection. The presence of two arcs can reflect grain interior and grain boundary resistances that are typically considered as electrically in series for samples without a conductive network (e.g., Huebner and Dillenburg, 1995; Roberts and Tyburczy, 1991). Electrode polarization may impact the very lowest frequencies of impedance spectra, and we have aimed to exclude this contribution from the analysis. The bulk resistance R specific to the sample is next determined after making minor corrections for the parallel resistance (very high) of the alumina ring, and for the series resistance (very low) of the two Fe-disk electrodes. The low-frequency conductivity of the sample, σ, or its inverse, resistivity ρ, is then obtained using the geometric factor G (=area/length ratio of the sample):

$$\sigma = \frac{1}{\rho} = \frac{1}{R \times G} \quad (1)$$

A typical value of G for our samples is 1.4×10^{-3} m.

The real conductivity is often referred to as the DC conductivity, though it is measured with low-frequency AC signals. Real conductivity values at higher frequencies, e.g., 10 or 100 kHz for which the resistance and capacitive reactance may both contribute substantially to the overall sample impedance, are calculated from Z', the modulus $|Z| = (Z'^2 + Z''^2)^{1/2}$, and G:

This is the peer-reviewed, final accepted version for American Mineralogist, published by the Mineralogical Society of America.
The published version is subject to change. Cite as Authors (Year) Title. American Mineralogist, in press.
DOI: https://doi.org/10.2138/am-2023-9054. http://www.minsocam.org/

206 $$\sigma' = \frac{Z'}{G|Z|^2} \quad (2)$$

207 Uncertainties in conductivity values were computed as described in Saxena et al. (2021), and
208 amount to less than ~10 % over the entire temperature range.

209

210 **Chemical and textural analyses**

211 Selected quenched samples were analyzed using the electron microprobe to characterize
212 the phases, composition, and texture. Electron microprobe analyses were performed with a field
213 emission electron microprobe (JEOL 8530F at the Carnegie Institution for Science). Analyses
214 were done with an acceleration voltage of 15 kV, and a sample current of 20 nA. Integration
215 times were 20 s on peak and 10 s on background, except Na and P which were analyzed with
216 50% shorter times. For a quenched melt, the beam was slightly defocused (~5 μm), and for
217 crystalline phases, the beam was focused to 1 μm. The following standards were used: albite
218 (Na), olivine (Fe, Mg, Si, Ni), anorthite (Ca, Al), TiO_2 (Ti), $MgCr_2O_4$ (Cr), Mn metal (Mn),
219 orthoclase (K), apatite (P), and pyrite (S) for the dunite, and pyrite (Fe, S), Ni metal (Ni), and
220 $MgCr_2O_4$ (O) for the sulfide phases.

221 In addition to spot analyses on the silicate and sulfide phases, wavelength dispersive
222 spectroscopy (WDS) was used to obtain chemical maps of selected samples. High-resolution
223 WDS maps used a 1-micron diameter beam and a 20-msec dwell time.

224

225

226 **RESULTS**

227 **Composition and texture of quenched samples**

Representative BSE images and WDS maps of quenched samples containing metal sulfides are shown in **Figures 1, 2** and **Figure S3**. At the sample scale, sulfide regions are well distributed, and no segregation of the sulfide phase is observed (see **Figure 1A** for a sample with 3.4 vol.% FeS, and **Figure S3** for samples with 3.4 or 6.5 vol.% Fe-S-Ni). The shapes of the metal sulfide blebs vary (**Figures 1B-1D**). Dihedral angles are not single-valued, consistent with expectations for a melt interacting with a variety of different crystallographic faces and planes of a natural rock (e.g., Kohlstedt, 2002). Some rounded sulfide blebs (high angles) are isolated in pockets in grain boundaries and triple junctions, whereas other sulfides appear interconnected along a few grain boundaries and triple junctions (low angles). Sulfide interconnection over tens of micrometers is rarely visible, and continuous conductive pathways can only be speculated from the 2-D BSE images. O-rich, S-free rounded grey grains contiguous to sulfide blebs are sometimes observed (**Figure 1B**) and are possibly iron oxides that precipitate upon quenching.

WDS maps of samples with metallic Ni (or, metallic Ni and Fe) as part of their composition indicate a high degree of overlap for Fe, S, and Ni (**Figure 2**), demonstrating that the initially pure-metal phases were mixed with FeS once the highest ~1600 K temperature was reached. Very few isolated Ni or Fe grains are observed in samples with added Ni or Fe metal, such as BB295 (**Figure 2C**). These grains could reflect a quenched texture, or perhaps slightly incomplete mixing.

Quantitative chemical analysis of the iron sulfide regions was challenging, given their small size and complex texture. Typically, only the largest metal sulfide phases of each sample were analyzed, and the values presented in **Table 2** should not be considered as representative of the bulk metal or sulfide content. The presence of regions with nearly pure iron and very little sulfide is not necessarily evidence of incomplete mixing, because phase separation during

quenching is likely. Most of the analyzed sulfide regions revealed significant amounts of O (1–4 wt.%; **Table 2**). The amounts of oxygen are similar to those reported in a previous study (Terasaki et al., 2005) for samples of olivine with Fe# 0.11, in equilibrium with a sulfide melt. However, olivine cannot be the primary source of oxygen, because the highest quantity (3.84%) is found for the pure FeS sample (BB280). Most likely the oxygen originates from other processes, possibly incorporation of water in the relatively soft sulfide phase during polishing, and incomplete drying before microanalysis. For experiments with added nickel (BB290, BB294, BB295, BB299), no regions with pure Ni are reported in **Table 2**, consistent with the mixing observed in **Figure 2**. For several experiments without added nickel (BB281, BB289, BB291, BB292), the microprobe data indicate small amounts of Ni (0.16 – 1.25 wt.%) present in the sulfide regions. In these cases, the Ni originates from the olivine matrix, quantified by microprobe analysis as high as ~0.4 wt.% NiO (**Table 3**). The equilibrium of Ni between sulfide and olivine has been extensively addressed (e.g., Brenan, 2003; Solferino et al., 2015). Temperatures higher than 1023 K are necessary for the transfer of Ni, as inferred from the very low levels (0.07 wt.%, **Table 2**) in the sulfides of two samples quenched directly after short or long annealing periods (BB303 and BB304).

Two distinct populations of olivine are observed in the quenched samples (**Table 3**), with FeO levels 13.1 – 15.2 wt.% in one, and 16.1 – 23.9 wt.% in the other. The first population is similar to olivine in the starting powder (~14 wt.% FeO). The second population is observed within a ~100-micron distance from the Fe electrodes, or near Fe-rich sulfides. The Mg# for pyroxenes ranges from 81 – 88 (**Table 3**). Pyroxenes contain small amounts of TiO_2 (0.16-1.85 wt.%). Chromite grains are visible in most xenoliths, but their small size (<1 micron) makes chemical analysis difficult.

Based on a combination of microscopic observations and chemical analyses, sample contamination during the conductivity measurements can be summarized as follows. First, regarding Al from the alumina sleeve, a very thin (< ~30 micron) and discontinuous Al-rich layer is observed at the sample-sleeve interface, resulting from Al diffusion into the sample at high temperature (e.g., electron microprobe data for BB291 in **Figure S4**). This layer has a negligible effect on the bulk electrical measurements (e.g., Pommier et al., 2019). Second, some Fe contamination from the electrode disks is visible in BSE images, as mentioned above. Electron microprobe traverses (**Figure S4**) quantify these changes, and show that samples quenched at our highest temperatures (e.g., BB289, 1627 K) have substantial Fe replacement for Mg over a range <100 μm from the electrode, whereas samples quenched at a relatively low temperature (e.g., BB304, 1023 K) are affected over a shorter distance. Within ~50-100 microns from the electrodes, the samples are slightly depleted in Ni, but the distribution of S appears to be unaffected (e.g., WDS maps of BB295; **Figure S3**). The electrical measurements of samples are expected to be affected only minimally (<10%) by Fe contamination, or siderophilic depletion of Ni associated with the electrodes.

Electrical characterization during annealing

The effect of annealing at 1023 K on the electrical properties of the dunite and dunite-sulfide samples was investigated by varying the duration from 3.5 – 27.4 hrs (**Table 1**). Examples of electrical data during annealing are presented in **Figure 3**. For experiments with pure dunite or with 3.4 vol.% FeS (without added Ni) there are similar patterns in the bulk resistance and impedance arc structure, represented by sample BB304 in this figure. During the initial 200 – 300 minutes (stage 1), the bulk resistance increases by a factor of roughly 3 – 10.

(We note that the higher 6.5 and 18.2 vol.% concentrations of FeS do not follow the pattern of 3.4 vol.%, and instead show a decline in resistance during stage 1.) Two impedance arcs are typically seen in the complex impedance spectra of pure dunite and 3.4 vol.% samples; arc 1 at high frequency and arc 2 at low frequency. Both arcs increase during stage 1. Samples that were annealed for more than 6 hours (pure dunite BB293; or 3.4 wt.% FeS BB292, BB304, and BB305) show a significant decrease in bulk resistance starting at 300 – 400 min, and extending to 500 – 600 min (stage 2). In the complex impedance plot, both arcs diminish in stage 2, especially the low-frequency arc 2. In stage 3, the sample resistance is relatively steady, though minor increases from ~600 – 1400 minutes were observed and attributed to temperature variations. A single arc dominates the complex impedance plot.

The experiments with added Ni/Fe metal, represented in **Figure 3** by BB295 (6.5 vol.% $Fe_{40}S_{40}Ni_{20}$), follow a slightly different pattern. Similar to the samples described above, during stage 1 (~200 minutes) the bulk resistance increases. Two arcs are apparent in the complex impedance plot, and both grow in amplitude (arc 1 more than arc 2). In stage 2 (~600 minutes), unlike the previous samples, bulk resistance continues to increase. Arc 1 expands, but arc 2 diminishes. During the final stage 3, further increases in resistance are relatively small, and a single arc dominates the impedance plot. Sample BB294 (3.4 vol.% $Fe_{40}S_{40}Ni_{20}$) is an exception: after the resistance rises during the first ~500 minutes, it declines at a rate that slows with time until the end of the 27-hr annealing.

Variable-temperature impedance measurements

Impedance data (Z' and Z'' for each frequency) during cooling and heating cycles are shown for all experiments in the **Supplemental Material**. Representative impedance spectra

collected at various temperatures after annealing are presented for selected samples in **Figure 4**. For the pure dunite and sulfide-bearing dunite samples up to 6.5 vol.% metal sulfide, complex impedance spectra at low temperatures (< 1273 K) consist of a single arc, and its size decreases as temperature increases. With increasing temperature (above ~1273 K), only a portion of the arc is visible, because of noise at high frequency. Pure metal sulfide samples and the sample containing 18.2 vol.% FeS have low resistance values and impedance spectra that are typical of conductors (no arc; Saxena et al., 2021).

Temperature-dependent conductivity values are shown in **Figures 5** and **6**. Arrhenius plots of log(conductivity) vs. inverse temperature are shown in **Figure S5**, and activation energies are listed in **Table 4**. The temperature-dependent conductivities and activation energies for the various samples are summarized as follows:

Pure dunite (BB283, BB293)

The dunite sample annealed for 4.5 hours (BB283) has conductivity values ranging from a low of ~10^{-5} S/m at 700 K, to a high and nearly constant value of ~6×10^{-2} S/m over the range 1300 – 1600 K. The rising portion can be fitted with two (apparent) activation energies, 0.85 and 1.7 eV. The sample annealed for 24.6 hours (BB293, **Figure 5B**) has >10 times higher conductivity than BB283 at the lowest temperatures (e.g., ~2×10^{-4} at 700 K), but values for both samples are similar for temperatures >1100 K. Apparent activation energies for BB293 range from 0.18 eV at lowest temperatures, to 1.6 eV.

Dunite + 3.4 vol.% FeS (BB281, BB292, BB305)

When compared with pure dunite samples with corresponding annealing times, the temperature-dependent conductivities of the samples with 3.4 vol.% FeS show a similar pattern,

This is the peer-reviewed, final accepted version for American Mineralogist, published by the Mineralogical Society of America.
The published version is subject to change. Cite as Authors (Year) Title. American Mineralogist, in press.
DOI: https://doi.org/10.2138/am-2023-9054. http://www.minsocam.org/

though slightly higher values. Specifically, sample BB281 (3.4 vol.% FeS, 5-hr anneal; **Figure 5A**) has a conductivity of ~10^{-4} S/m at 700 K, a rise to ~0.1 S/m at ~1300 K, where it remains roughly constant until 1525 K. Apparent activation energies on the rising portion range from 0.14 to 1.9 eV. One clear difference between the conductivity profile for BB281 and the corresponding experiment with pure dunite (BB283, 4.5-hr anneal), is the steep increase over 1550 – 1620 K, to a high value of 0.7 S/m. Samples annealed for 5 vs. 24 hours are also compared in **Figure 5A**. The 24-hr annealed samples (BB292, BB305) have significantly higher conductivities at low temperature, but values converge with those of the 5-hr annealed sample BB281 at ~1100 K. The comparison is analogous to that described for pure dunite samples. Unlike sample BB281, a sharp rise is not seen for BB292 over the range 1550 -1600 K.

Dunite + 6.5 vol.% FeS (BB 289) and dunite + 18.2 vol.% FeS (BB291)

Samples with 6.5 or 18.2 vol.% FeS exhibit large differences in conductivity relative to pure dunite or samples containing 3.4 vol.% FeS (**Figure 6**). The 6.5 vol.% sample (BB289) has a conductivity ~0.04 S/m at 700 K, a gradual rise (E_a = 0.16 eV) to 0.1 S/m at 1050 K, then a much steeper rise (E_a = 2.4 eV) to a relatively steady maximum of ~4 – 7 S/m over the range 1200 - 1400 K. A sharp drop to ~1 S/m is noted from 1420 – 1480 K, and high values of 4 – 8 S/m are restored over the highest temperature range 1500 – 1630 K. The sample with 18.2 vol.% FeS (BB291) is characterized by high conductivity values across the full range, from ~60 S/m at 700 K to ~500 S/m at 1620 K, though all are at least 100× below the conductivity of pure FeS at the same temperature. Changes with temperature for the 18.2 vol.% sample are very gradual or flat over the range 670 – 1220 K and 1320 – 1620 K, with apparent activation energies mainly at

levels of 0.1 eV or less. The most substantial change is a gradual increase in conductivity over 1220 – 1320 K, spanning the FeS eutectic temperature.

Dunite + 3.0–3.4 vol.% Fe-S-Ni (BB290, BB299, BB294) and 6.5 vol.% Fe-S-Ni (BB295)

The conductivity curves for samples containing Fe-S-Ni over temperatures <1450 K are lower than those of pure dunite annealed for similar duration (**Figure 6**). Specifically, BB299 (3.4 vol.% $Fe_{50}S_{40}Ni_{10}$, 27-hr anneal) has the lowest conductivity of all samples in the dataset up to 1500 K, e.g., the value 10^{-6} S/m at 700 K is more than 100× smaller than that of the dunite sample BB293, annealed for a similar duration. As temperature increases, the conductivity of BB299 rises, with dominant activation energies 1.1 and 1.9 eV, to a value of ~2×10^{-2} S/m at 1350 – 1470 K. An additional small rise is observed over the range 1470 – 1570 K, and the sample slightly exceeds the conductivity of pure dunite at temperatures exceeding 1520 K. Sample BB290 has nearly the same quantity of $Fe_{50}S_{40}Ni_{10}$ (3.0 vol.%) as BB299, however it was annealed for only 6 hours. The conductivity values for BB290 are slightly lower than those of corresponding dunite sample, BB283 (annealed 5 hr), for all temperatures below 1500 K. As with sample BB299, sample BB290 slightly exceeds the conductivity of the pure dunite at the highest scanned temperatures 1500 – 1620 K. The sample BB294 (3.4 vol.% $Fe_{40}S_{40}Ni_{20}$, 27-hr anneal) has similar conductivity profile to pure dunite sample BB293, and once again, values are lower from 620 – 1400 K. Though sample BB295 (6.5 vol.% $Fe_{40}S_{40}Ni_{20}$, 27-hr anneal) has more sulfide than BB294, the former is less conductive for temperatures less than 900 K. Both samples reach a conductivity plateau of ~4×10^{-2} S/m, then exhibit a steep rise to values between 1 – 10 S/m. The rise for BB295 is particularly steep near 1500 K, and near 1580 K for BB294.

DISCUSSION

Numerous laboratory studies on metal sulfides in silicates have explored the connectivity of the sulfide phase by focusing on textural properties, particularly wetting angles of the solid/liquid interface. These studies, now including powerful 3-D tomographic techniques, are a continuing source of insights (e.g., Watson and Roberts, 2011; Solferino et al., 2020 and references therein). By comparison, laboratory electrical studies have been sparse, despite advantages which include important links to field measurements.

Consideration of oxygen fugacity

The fugacity of oxygen is well recognized to be influential in conductivity measurements of olivine or dunite (Schock et al., 1989; Wanamaker and Duba, 1993; Wanamaker, 1994) and various studies of sulfide melt inclusions (e.g., Rose and Brenan, 2001; Terasaki et al., 2005, 2008). Given that the COMPRES cell assembly is not designed for oxygen buffering, it is unlikely that the fugacity of the sample volume would be well controlled. Nevertheless, relatively reducing conditions are expected, given our choice of iron as the electrode material. The experimental approach can be compared with others at elevated pressure and temperature where metallic iron, without added iron oxide, was reported to achieve reducing conditions. These prior studies include analogous electrical conductivity measurements using Fe electrodes (Katsura et al., 2007), samples enclosed within an iron capsule or tube (Karato et al., 1986; Faul et al., 2018), or samples surrounded by a pressure medium doped with iron particles (Dobson and Brodholt, 1999). For the present study, the commonly used molybdenum metal was a possible alternative metal for the electrodes, and has been shown or suggested to achieve low fugacity values close to the iron-wüstite buffer (e.g., Xu et al., 1998; Katsura et al., 2007; Yoshino, 2010;

411 Watson and Roberts, 2011; Dai and Karato, 2014). However, given uncertainty in the
412 performance of Mo/MoO_2 buffer below 1150 K (O'Neill, 1986), iron was considered a better
413 choice for influencing the oxygen fugacity at and below the 1023 K annealing temperature.

414 Other factors which affect oxygen fugacity within the sample include the metallic Ni and
415 Fe particles added in four experiments, as well as several reactions in the dunite host involving
416 Fe_2SiO_4, Mg_2SiO_4, SiO_2, and orthopyroxene (e.g., Karato et al., 1986; reactions 1 – 3 in Rubie et
417 al., 1993; reactions 1 and 5 of Faul et al., 2018).

418

419 **Electrical properties during annealing**

420 The effect of annealing on electrical properties of geomaterials is not commonly
421 presented in depth and has not been investigated for sulfide-bearing silicate rocks. From our
422 electrical results, three stages can be suggested.

423 *Stage 1*:

424 The relatively rapid increase in bulk sample resistance during stage 1, for all runs except
425 for 6.5 and 18.2 vol.% FeS, is most likely caused by loss of adsorbed water from the sample and
426 other cell parts. This behavior is frequently observed (Yoshino, 2010), particularly in studies
427 involving powdered samples (e.g., Manthilake et al., 2015; Huang et al., 2021). Assuming the
428 validity of modeling grain interior and boundary as resistors in series (e.g., Roberts and
429 Tyburczy, 1991; Yoshino, 2010) the growth of both arc 1 and 2 during stage 1 indicates that
430 dehydration increases the resistance of both portions of our samples.

431 *Stage 2*:

432 The hallmarks of this stage include (1) loss or minimization of the low-frequency arc; (2)
433 a significant and relatively steep decrease in bulk resistance for pure dunite and mixed samples

434 with 3.4 vol.% FeS; (3) a slow increase in bulk resistance for 3.4 vol.% Fe-S-Ni samples. Three
435 mechanisms may contribute to the behavior in stage 2. Any of these may have also been active
436 during stage 1, but overshadowed by the effects of dehydration.

437 First, the sample porosity could decrease during stage 2 simply as a consequence of the
438 applied pressure and elevated temperature. Lower porosity would be expected to lower bulk
439 resistivity. However, decreased porosity alone does not provide a clear explanation for the
440 changes in impedance arc structure. Also, this mechanism does not seem consistent with the
441 similar responses of pure dunite and 3.4 vol.% FeS mixed samples, vs. the different response of
442 3.4 vol.% Fe-S-Ni samples.

443 Second, the application of 2-GPa pressure and 1023-K temperature over 6 – 10 hours
444 may have decreased the inter-grain resistance to such an extent that arc 2 (assigned to grain
445 boundaries) becomes minimal or disappears entirely. This explanation agrees with pressure
446 effects proposed earlier: by comparing impedance spectra of silicates acquired at ambient
447 pressure (showing two arcs) vs. at 2 – 20 GPa (showing one arc) the conclusion was reached that
448 grain boundary resistance can become negligible at high pressure (e.g., Huebner and Dillenburg,
449 1995; Poe and Xu, 1999). Our work builds on this proposal, by showing how the arcs can evolve
450 as a function of time while a sample is under pressure at a modest annealing temperature.
451 However, this mechanism does not explain all aspects of stage 2; for example, the reason for a
452 decrease in grain interior resistance (arc 1) is not addressed.

453 Third, the change in bulk resistance could reflect the chemical response of the sample to
454 changes in oxygen fugacity. The initial heating from 298 to 1023 K was relatively rapid (40
455 min), and the sample must equilibrate with a greatly increased oxygen fugacity concomitant with
456 this temperature rise. Olivine samples have been reported to take hours to equilibrate with

457 fugacity changes (e.g., Schock et al., 1989; Wanamaker and Duba, 1993; Wanamaker, 1994). We
458 speculate that the decline in resistance could be caused by the slow formation of polaron defects
459 as the dehydrated sample reaches equilibrium with the higher oxygen fugacity. This explanation
460 is consistent with the difference in behavior caused by changes in metal sulfide composition.
461 When Fe or Ni metal particles are dispersed throughout the sample, they can counteract the more
462 oxidizing environment and limit the formation of conductive polarons. Like the previous
463 mechanism, this one does not explain all aspects of stage 2, particularly the loss of one
464 impedance arc.

465 To summarize, much of the electrical behavior shown in stage 2 can be explained by the
466 second mechanism (decreased inter-grain resistance caused by pressure and temperature) in
467 combination with the third mechanism (chemical equilibration of the sample to increased oxygen
468 fugacity).

469 *Stage 3*

470 Electrical changes in stage 3 are minimal. We interpret the stabilization in bulk resistance
471 as the attainment of a certain degree of textural and chemical equilibrium at 1023 K. This
472 equilibrium should be viewed in the context of 5 – 27 hour annealing times. Further changes in
473 the electrical response would be expected if the annealing were extended many days (or longer),
474 e.g., as slow grain growth modifies the sample (Karato, 1989; Nichols and Mackwell, 1991;
475 Solferino et al., 2015; Solferino and Golabek, 2018).

476

477 **Electrical properties at low frequency, based on variable-temperature scans**

478 *Pure dunite*

As host for the metal sulfide, dunite is important for establishing the conductivity of the bulk sample. The pair of conductivity curves for dunite (BB283, annealed for 4.5 hrs; BB293 annealed for 24.6 hrs) are clearly the "parent" curves of all samples containing 3.0 or 3.4 vol.% FeS or Fe-S-Ni. One can consider the various ~3 vol.% metal sulfide mixes as a perturbation to the pure dunite; thus, an understanding of the dunite-only variable-temperature conductivity profiles directly impacts an understanding of the mixtures.

There are several noteworthy features in the conductivity trends of the pure dunite. For example, the conductivities measured in both experiments are unusually high, and the activation energies are low, compared with olivine samples containing similar iron content and low levels of volatiles (e.g., Poe et al., 2010; Yoshino et al., 2006, 2012). Volatiles may explain some aspects of the dunite conductivity curves, but a full analysis extends beyond the scope of the present work. More importantly, we note that the changes caused by annealing the dunite sample for 24.6 hours (BB293) rather than 4.5 hours (BB283), specifically the nearly 10× increase in conductivity at lowest temperature, and extraordinarily low activation energies (0.18 and 0.56 eV, rather than 0.86 eV) cannot be explained in terms of volatiles. During a longer annealing time, water content in the unsealed sample space should decrease, and the quantity of other possible conductive impurities, particularly graphitic carbon, should either remain the same or decrease. Loss of volatiles with longer annealing times would decrease conductivity and increase activation energy, opposite of the changes observed for BB293. This comparison strongly suggests that another factor impacts the variable-temperature resistivity profiles.

Additionally, the nearly flat conductivity values over the temperature range 1300 – 1600 K are very unusual for a silicate sample. Silicates with extensive melting can display a relatively weak dependence of conductivity on temperature (e.g., Rai and Manghnani, 1978; Maumus et

al., 2005; Ni et al., 2011; Pommier et al., 2015). However, partial melting is not realistic for the dunite sample over the investigated temperature range. The estimated solidus temperature at 2 GPa for xenoliths of this type is close to 1650 K (see Figures 10 and 13 of Gibson et al., 2013), and no evidence for melting is visible from the SEM images of quenched samples. The flat conductivity profile at high temperatures suggests once again that some other factor, not volatiles or partial melting, has a strong effect.

The comparisons between BB283 and BB293 suggest that the scans to lower temperature (at an average rate –7 K/min) are not fully equilibrated, e.g., with oxygen fugacity as it drops upon cooling. Defects that are generated during annealing, especially for the longer duration, are likely to persist upon cooling and contribute to the conductivity. Olivine samples have been reported to take hours to re-equilibrate, particularly at temperatures below 1270 K (Wanamaker and Duba, 1993; Poe and Xu, 1999). Similarly, the flat conductivity profiles above ~1300 K, measured at an average heating rate of +5 K/min, are likely affected by a lack of equilibration. Oxygen fugacity is expected to rise with temperature, and for an equilibrated sample, increased fugacity is known to enhance the concentration of Fe^{3+} polarons (e.g., Schock et al., 1989; Hirsch and Shankland, 1993) and consequently the conductivity. If the sample chemistry evolves too slowly, then the typical conductivity increase associated with raising temperature will not be achieved.

Regardless of the detailed explanations for the characteristics of the two dunite conductivity curves, a key point is that each one serves as a reference for the sulfide-dunite samples. Sample BB283 was annealed only for a period as long as stage 1; by cutting short stage 2, this sample does not undergo the resistivity drop (conductivity rise) as BB293 does. To make

524 the best comparisons, mixture samples should be compared with the respective dunite sample
525 that was annealed for the same or similar duration.
526
527 *Dunite + 3.4 % FeS*
528 Overall, the variable-temperature measurements of these samples (BB281 with 5-hr
529 annealing; BB292 and BB305 with ~24-hr annealing) are not surprising. Each sample shows
530 slightly higher conductivity values, relative to the respective pure-dunite samples. The improved
531 conductivity is understandable for a mixture of a dilute, disconnected conductive phase in the
532 midst of a poor one. The only unusual aspect of this sample set is the conductivity jump observed
533 for BB281 from 1550 K to the quench temperature 1620 K. The high point (~0.7 S/m) is more
534 than 10× greater than the pure dunite, and indicates that some degree of connectivity was
535 achieved with this sample.
536
537 *Dunite + 6.5 vol.% and 18 vol.% FeS*
538 Experiment BB289 (6.5 vol.% FeS, 5-hour dwell) is exceptional, with conductivity
539 values that are at least 10× greater than the respective pure-dunite sample for all scanned
540 temperatures, including those for which the FeS is solid or molten. Over a temperature variation
541 that exceeds 1000 K, the conductivity range of this sample varies by less than a factor of 400.
542 Such little variation is uncharacteristic of the silicate host. Additionally, there is a dramatic ~1.5-
543 log unit increase in conductivity over 1100 - 1200 K, below the eutectic temperature.
544 These observations indicate that a small fraction of FeS forms a percolative path through
545 the sample. At low temperatures, increases in conductivity by factors of 100 – 1000 relative to
546 the pure dunite suggest that such a network forms even when the sample is solid. The sudden

increase in conductivity over the 1100 – 1200 K range is likely caused by softening of FeS, which in turn causes an even greater fraction of the metal sulfide to become connected. FeS is known as an exceptionally soft material (e.g., compared with pyrite) near and below the eutectic temperature of 1260 K (Buseck, 1977; Graf and Skinner, 1970).

Similar points relating the connectivity of the FeS to its deformable (plastic) nature were expressed by Bagdassarov et al. (2009a). To the best of our understanding of the conductivity vs. 1/T trajectories presented in the prior work, samples with all concentrations of $Fe_{57}S_{43}$ (at.%) in either peridotite or olivine had high and flat conductivity profiles at the outset, before the first heating to ~1250 K (Figures 4 and 5 in Bagdassarov et al., 2009a). If correct, then some aspect of preparatory steps in this work yielded a very different outcome than observed in the present study. Our findings are more closely related to those of Yoshino et al. (2003, 2004) which show increases in conductivity as the sample approaches the eutectic melting temperature.

Upon crossing the eutectic temperature at 1260 K, the conductivity of our 6.5 vol.% sample hardly increases. The work of Yoshino et al. for 6 and 12 vol.% samples may have similar characteristics, though the background caused by conduction through the BN sample container makes this comparison difficult. The observations from our study clearly indicate that when FeS is in a softened solid state, it forms connections that are possibly analogous to those when it is molten. At greater temperatures, specifically 1400 - 1500 K, the significant drop in conductivity suggests that the network formed when 6.5 vol.% FeS is molten is not robust. This observation is consistent with a tendency of the sulfide melt to avoid interconnection, particularly with accelerated grain growth of the host caused by a substantial ΔT above the annealing temperature (Walte et al., 2007; Bagdassarov et al., 2009a; Solferino et al., 2020). For temperatures exceeding 1500 K, the relatively high conductivity of the 6.5 vol.% FeS sample is

restored. The cause is uncertain, but one possibility is that the temperature is then sufficient to drive iron from the FeS melt into the olivine matrix (supported by **Table 3**). Increased iron content in olivine would enhance its conductivity (e.g., Yoshino et al., 2012) and would lower the amount of metal-sulfide that is necessary for connectivity (Terasaki et al., 2005). Despite uncertainty in the mechanisms for conductivity increases or decreases for this particular sample, the 6.5 vol.% composition is exceptional in displaying characteristics of a fragile metal-sulfide network.

The 18.2 vol.% sample is undoubtedly above the percolation threshold across the entire temperature range, as evidenced by the nearly temperature-independent behavior, and conductivity values that are at least 1000 times higher than the pure dunite run over the entire temperature scan. The gradual 4× increase in conductivity centered around the FeS eutectic is only partly explained by a 1.5× conductivity increase that is expected of the pure FeS (Saxena et al., 2021). Apparently, there is also some improvement in the metal-sulfide connectivity upon melting this portion of the 18.2 vol.% mixture. Unlike the sample with 6.5 vol.%, the elevated conductivity is maintained throughout the full range of temperatures. For the portion of the curves with overlapping temperatures, the behavior of our 18 vol.% sample agrees with the relatively flat conductivity line at ~10^2 S/m shown for the same concentration in Yoshino et al. (2004).

The heating curve for the 17.5 vol.% shown in Bagdassarov et al. (2009a) also agrees with our finding for 18.2 vol.% FeS over relatively low temperatures, however neither we nor Yoshino et al. (2004) observed a drop-off in conductivity matching that in the 2009 study. In our work, the scan through high temperatures is shorter than the times that Bagdassarov et al.

592 (2009a) state as necessary to disrupt the interconnectivity of the melt. Possibly with a sufficient
593 waiting period we would see a decline as well.
594
595 *Dunite + Fe-S-Ni*
596 Nickel could influence the conductivity in a variety of ways. If the FeS, Ni, and Fe
597 particles combined at relatively low temperatures, the eutectic temperature could drop
598 substantially, according to some studies. For example, Beyer et al. (2022) have reported that an
599 increase in Ni content from 6.3 to 25.7 wt.%, for a nearly fixed atomic ratio of total metal/sulfide
600 (0.91 or 0.92), decreases the solidus temperature by 140 K at either 0.1 MPa or 2 GPa. Although
601 these compositions from Beyer et al. (2022) are not the same as the $Fe_{50}S_{40}Ni_{10}$ and $Fe_{40}S_{40}Ni_{20}$
602 samples in the present study, nevertheless one might expect that at least $Fe_{40}S_{40}Ni_{20}$ would have
603 a lower eutectic point relative to FeS. (However, we note that results from Usselman (1975)
604 indicate only minor changes in eutectic temperature for 6.5 wt.% quantities of Ni in comparison
605 to Ni-free sample, at least for pressures from 0.1 MPa to 6 GPa, and no comparison with results
606 reported by Beyer et al. (2022) has been made so far). More importantly, we must question when
607 Ni first incorporated in FeS for our samples. Though the quenched Fe-S-Ni samples showed
608 effective mixing once the final ~1600 K quenching temperature was reached, we have no
609 evidence that FeS, Fe, and Ni particles mixed effectively at relatively low temperatures. It would
610 seem more reasonable to expect that the FeS grains first underwent partial or full melting before
611 this phase combined with solid Ni grains (or Fe grains, for samples with 10 wt.% Ni). If this
612 scenario were correct, any potential lowering of the eutectic temperature for the Fe-S-Ni
613 mixtures would not be realized.

614 Over any temperature range for which Ni (or Fe) particles remained unmixed with FeS,
615 one might simply expect that the high conductivity of pure Ni (at least 2.5×10^6 S/m for
616 temperatures less than 1000 K and presssures 1 atm – 3 GPa; Silber et al., 2017) to cause these
617 samples to be better conductors overall, relative to those with only FeS (~10^5 S/m). However,
618 two factors prevent this from happening. First, the total content of Ni is on the order of 1 vol.%
619 (at most 20% of 6.5 vol.%), which would typically be too low to form a conductive network.
620 Second, the melting point of metallic Ni at 2 GPa is between ~1730 K (1 atm) and ~1760 K (3
621 GPa) (Silber et al., 2017), which suggests that it does not soften or become plastic until much
622 higher temperatures than FeS. Taken together, the small quantity and hardness of Ni relative to
623 FeS appear to overshadow the improved conductivity of Ni.
624 The samples with added metallic iron display the lowest electrical conductivity (BB290,
625 and especially BB299), which suggests that the incorporated Fe effectively lowers oxygen
626 fugacity throughout the sample, and thereby minimizes the quantity of Fe^{3+} polarons. Addition of
627 nickel without iron particles (BB294, BB295) also causes reducing conditions but the effect is
628 not as strong. This trend is fully consistent with the well-known impact of nickel/nickel oxide vs.
629 iron/wüstite buffers on oxygen fugacity.
630 Once temperatures are in the 1500-1600 K range or higher, the conductivity increases for
631 samples BB294 and BB295 could be explained by increased plasticity of the Ni phase, and
632 ultimately a merging of Ni and metal sulfide phases to form a Fe-S-Ni melt as seen in the images
633 of quenched samples. Prior work (Rose and Brenan, 2001) has shown that the addition of Ni to
634 an FeS melt hosted by olivine yields higher dihedral angles, particularly at low oxygen
635 fugacities, which counteracts wetting and interconnection of the melt. This low wettability is
636 possibly a key factor which renders the 6.5 wt.% sample of Fe-S-Ni (BB295) considerably less

637 conductive than the 6.5 wt.% sample of FeS (BB289). Overall, the Fe-S-Ni experiments are best
638 to consider as preliminary work because of the numerous influences discussed above, the
639 complexity associated with a non-uniform metal-sulfide phase, and additional factors such as
640 interdiffusion of Ni between the olivine host and the metal sulfide (**Table 2**).
641
642 **Re-evaluation of electrical connectivity in dunite-sulfide mixtures**
643 The electrical measurements presented here and previously (Saxena et al., 2021) yield
644 conductivity values of mixed samples that are at least 100× lower than those of the pure FeS
645 sample across the investigated temperature range (650 – 1630 K). To quantify the level of
646 connectedness, we previously modeled the conductivity values at selected temperatures, using
647 the Hashin-Shtrikman upper and lower bounds, as well as the empirically-derived modified
648 Archie's law (Glover, 2015). An unusually high cementation exponent (4 to 5) was necessary,
649 suggesting that the conductive phase is almost entirely disconnected (see Table 3 in Glover,
650 2015). An alternative and more straightforward approach involves applying a model modified
651 from Waff (Bahr, 1997) with the following equation:
652 $$\sigma_{bulk} = \frac{2}{3} \times X_{FeS} \times \sigma_{FeS} \times \gamma \quad (3)$$
653 Here, X_{FeS} is the volume fraction of FeS, and γ is an electrical connectivity parameter ranging
654 from 0 to 1. Equation 3 leads to an analogous conclusion as found by applying other models: the
655 conductivities of the mixed samples, relative to the pure FeS, are only consistent if γ is small.
656 Specifically, for the 6.5% FeS sample, the highest connectivity parameter γ is 0.001 (0.1%), and
657 even for the 18 vol.% metal-sulfide sample, the highest γ, either below or above the eutectic
658 temperature, is 2.5%. Even our most concentrated mixed sample with 18.2 vol.% metal sulfide –

and certainly the one with 6.5 vol.% – is accurately described as highly disconnected rather than interconnected.

Extension of conductivity measurements to frequencies > 1 kHz

The acquisition and analysis of both real and imaginary impedance spectra from frequencies sub-1 Hz to MHz or beyond has been shown to yield insights into diverse materials and physicochemical processes (e.g., Jonscher, 1999; Gerhardt, 2005 and references therein; Barsoukov and Macdonald, 2018). For samples probed in large-volume presses, scans over a wide range of frequency (<1 Hz to >1 MHz), are typically analyzed to extract a very small number of real conductivity values (i.e., intersections with the Z′ axis), and most commonly only the extrapolated DC value is considered useful. Although this approach has yielded many insights into electric behavior (e.g., Yoshino, 2010; Pommier, 2014; Dai et al., 2020), it also represents a significantly constrained use of the technique, which would otherwise yield insights that extend well beyond DC behavior (e.g., dielectric properties). In the present study, we aimed to extract a complete set of frequency-dependent complex conductivity and permittivity data.

As described below, this goal was hindered by technical challenges. The departure of conductivities measured at high frequency relative to low or DC (**Figure 7**) could be interpreted as evidence that charge transport is more facile at high frequency, as has long been observed for rock or mineral samples (e.g., Fuller and Ward, 1970). However, three points support a case that impedances separate from the sample itself have a significant influence on the AC response. First, despite orders of magnitude variation in DC conductivity at low temperatures (e.g., near 673 K), as expected for the dissimilar materials, the values for real resistivity approach a plateau value that is remarkably similar (ranging from 0.45 to 1.5 mS/m) for the samples. This

This is the peer-reviewed, final accepted version for American Mineralogist, published by the Mineralogical Society of America.
The published version is subject to change. Cite as Authors (Year) Title. American Mineralogist, in press.
DOI: https://doi.org/10.2138/am-2023-9054. http://www.minsocam.org/

convergence for very different samples seems unlikely. Second, the lowest conductivity at 100 kHz (~0.45 mS/m for BB299) corresponds to an impedance of 1.6 MΩ, assuming a geometric factor of 0.0014 m. This impedance is presented as real in **Figure 7**, however, we note that a capacitive reactance (imaginary) would have a value of 1.6 MΩ ($X_c = 1/2\pi fC$) for a 1 pF capacitor at 100 kHz. The probe wires, coupled to the many grounded surfaces in the multianvil press, could achieve such a capacitance. This proposal raises the question how a capacitive reactance would manifest as a real resistance in our measurements. Studies exploring apparent inductance loops in impedance spectroscopy have highlighted that stray capacitance, particularly with a 4-point measurement, can cause unexpected phase shifts (Fleig et al., 1996). Possibly, stray capacitance in our setup is located so that the typical phase shift of $-\pi/2$ appears differently. Third, we note that as frequency $f = 2\pi\omega$ increases to 1 MHz, the real relative permittivity $\varepsilon'(\omega)$ computed from the impedance $Z^*(\omega)$, geometric factor G, and the vacuum permittivity ε_0,

$$\varepsilon'(\omega) = \frac{-Z''}{\omega\, G\varepsilon_0 |Z|^2} \quad (4)$$

is ~1000. Values for the apparent real relative permittivity as high or even much higher than 1000 are not unusual at low (e.g., 1 - 100 Hz) frequencies, when space-charge effects are dominant (e.g., Fuller and Ward, 1970). However, at 1 MHz when space-charge processes are too slow to respond to the rapidly oscillating field, rocks or minerals that have minimal water content are expected to have $\varepsilon'(\omega)$ values in the range 1 - 10 (e.g., Olhoeft, 1989). A value of 1000 is physically unreasonable at these frequencies. An extraneous capacitance on the order of 1 - 10 pF, dominating the expected sample capacitance of 0.01 – 0.1 pF, may be the cause. Minimization or compensation for the capacitive coupling across the full frequency sweep may

be a substantial challenge in typical multianvil setups, given proximity of sample and furnace, between pairs of probe wires, or between grounded parts of the press and each probe wire.

IMPLICATIONS

Over the past two decades, electrical and permeability studies of metal sulfides in silicates have presented differing views regarding the level of interconnectivity. Some reports have emphasized the disconnectedness of the metal sulfide phase, and support a relatively high percentage (~14-18 vol.%) as a percolation threshold (Bagdassarov et al., 2009a,b; Solferino et al., 2020). Others are consistent with significantly lower percolation thresholds of ~6 vol.% (Yoshino et al., 2003, 2004; Watson and Roberts, 2011). One implication based on our findings is that there may be more points of agreement than has been expressed previously. Though we agree with the majority of electrical studies which highlight an iron sulfide quantity of ~6 vol.% as an important threshold, nevertheless the unstable or fragile connectivity of our 6.5 vol.% sample also validates some points raised by Bagdassarov et al. (2009a). Additionally, we highlight that the vast majority of metal sulfide, even at the highest level within the mixed samples of our study (18 %) and comparable ones, is not part of a viable conduction path.

Our findings also imply that interconnectivity of molten metal sulfide is not the only focal point for understanding the bulk electrical conductivity of metal sulfide/olivine mixtures. The fact that the two mixed samples with the highest conductivities (6.5 and 18 vol.% FeS) show similar bulk conductivity below and above the eutectic temperature strongly suggests that new lessons may be derived from examining connectivity in the fully solid state, and by comparing with the state for which the conductive phase is molten. More generally, the present work is another contribution to a growing number of high-P and variable-T electrical studies focused on

mixed samples containing olivine and a much more conductive solid phase, e.g., magnetite (Dai et al., 2019), chromite (Sun et al., 2021), or ilmenite (Sun et al., 2022). As generalizations develop from this body of work regarding threshold quantities, or the range of conductivity variation with quantity, it is reasonable to anticipate fruitful extensions or comparisons with systems containing a molten conductive phase.

In the field, high electrical conductivity anomalies observed in cratonic contexts at a depth <100 km have been interpreted in terms of small amounts of metallic sulfides (e.g., Evans et al., 2011; Saxena et al., 2021; Bedrosian and Frost, 2022). Our results suggest that iron sulfide is a plausible candidate to explain some high-conductivity (>0.1 S/m) anomalies observed in Tanzania (Selway, 2014), Kaapvaal (Evans et al., 2011), Gawler cratons (Thiel and Heinson, 2013), and the Wyoming Province (Bedrosian and Frost, 2022). However, metal sulfides in natural settings are rarely FeS (e.g., Fleet and Stone, 1990; Wang et al., 2010). The preliminary work presented here on more realistic compositions ($Fe_{50}S_{40}Ni_{10}$ and $Fe_{40}S_{40}Ni_{20}$) suggests that stoichiometric FeS is possibly not an adequate proxy for these compositions. When excess metal (Fe and/or Ni) is added to the sulfide, the reducing influence on the host is significant.

Acknowledgements

The authors are grateful to Carnegie-EPL librarians M.A. O'Donnell and Shaun Hardy for their assistance. We thank G. Solferino for an extensive review, as well as L. Dai and three anonymous reviewers for their helpful feedback.

Funding

AP acknowledges support from NSF-CAREER award EAR-1750746. Use of the COMPRES Cell Assembly Project was supported by COMPRES under NSF Cooperative Agreement EAR 1661511. The electrical cell used in these experiments is available via COMPRES.

References

Anderson, L.A., Electrical properties of sulfide ores in igneous and metamorphic rocks near East Union, Maine. (1960) Geological Survey Research 1960; Short papers in the geological sciences, 400-B, pp. B125 – B129. https://pubs.er.usgs.gov/publication/pp400B

Aulbach, S., Griffin, W.L., Pearson, N.J., O'Reilly, S.Y., Kivi, K., and Doyle, B.J. (2004) Mantle formation and evolution, Slave Craton: Constraints from HSE abundances and Re–Os isotope systematics of sulfide inclusions in mantle xenocrysts. Chemical Geology, 208, 61–88. https://doi.org/10.1016/j.chemgeo.2004.04.006

Bagdassarov, N., Golabek, G.J., Solferino, G., and Schmidt, M.W. (2009a) Constraints on the Fe–S melt connectivity in mantle silicates from electrical impedance measurements. Physics of the Earth and Planetary Interiors, 177, 139 – 146. https://doi.org/10.1016/j.pepi.2009.08.003

Bagdassarov, N., Solferino, G., Golabek, G. J., and Schmidt, M. W. (2009b) Centrifuge assisted percolation of Fe-S melts in partially molten peridotite: Time constraints for planetary core formation. Earth and Planetary Science Letters, 288, 84–95. https://doi.org/10.1016/j.epsl.2009.09.010

Bahr, K. (1997) Electrical anisotropy and conductivity distribution functions of fractal random networks and of the crust: the scale effect of connectivity . Geophysical Journal International, 130 (3) 649 – 660. https://doi.org/10.1111/j.1365-246X.1997.tb01859.x

Barnes, S.J., Holwell, D.A., and Le Vaillant, M. (2017) Magmatic sulfide ore deposits. Elements, 13(2), 89-95. https://doi.org/10.2113/gselements.13.2.89

Barsoukov, E., and Macdonald, J.R. (2018) Impedance Spectroscopy: Theory, Experiment, and Applications, Third Edition, J. Wiley & Sons, Inc., 528 pp., doi:10.1002/9781119381860

Bedrosian, P.A., and Frost, C.D. (2022) Geophysical extent of the Wyoming Province, western USA: Insights into ancient subduction and craton stability. GSA Bulletin ; https://doi.org/10.1130/B36417.1

Beyer, C., Bissbort, T., Hartmann, R., Berndt, J., Klemme, S., and Fonseca, R.O.C. (2022) High-pressure phase relations in the system Fe–Ni–Cu–S up to 14 GPa: implications for the stability of sulfides in the earth's upper mantle. Contributions to Mineralogy and Petrology, 177, 99. https://doi.org/10.1007/s00410-022-01966-x

Brenan, J.M. (2003) Effects of fO_2, fS_2, temperature, and melt composition on Fe-Ni exchange between olivine and sulfide liquid: Implications for natural olivine–sulfide assemblages. Geochimica et Cosmochimica Acta, 67 (14), 2663–2681.

Brett, R., and Bell, P.M. (1969) Melting relations in the Fe-rich portion of the system Fe-FeS at 30 kb pressure. Earth and Planetary Science Letters, 6 (6), 479 – 482. https://doi.org/10.1016/0012-821X(69)90119-8

Buseck, P.R. (1977) Pallasite meteorites–mineralogy, petrology, and geochemistry. Geochimica et Cosmochimica Acta, 41, 711 – 740. https://doi.org/10.1016/0016-7037(77)90044-8

Chin, E. J. (2018) Deep crustal cumulates reflect patterns of continental rift volcanism beneath Tanzania. Contributions to Mineralogy and Petrology, 173: 85. https://doi.org/10.1007/s00410-018-1512-z

Dai, L., Hu, H., Jiang, J., Sun, W., Li, H., Wang, M., Vallianatos, F., and Saltas, V. (2020) An overview of the experimental studies on the electrical conductivity of major minerals in the upper mantle and transition zone. Materials, 13 (2), 408. https://doi.org/10.3390/ma13020408

Dai, L., Hu, H., Sun, W., Li, H., Liu, C., and Wang, M. (2019) Influence of high conductive magnetite impurity on the electrical conductivity of dry olivine aggregates at high temperature and high pressure. Minerals, 9(1), 44. https://doi.org/10.3390/min9010044

804 Dai, L., and Karato, S. (2014) Influence of oxygen fugacity on the electrical conductivity
805 of hydrous olivine: Implications for the mechanism of conduction. Physics of the Earth and
806 Planetary Interiors, 232, 57-60. https://doi.org/10.1016/j.pepi.2014.04.003
807 Delpech, G., Lorand, J.-P., Grégoire, M., Cottin, J.-Y., and O'Reilly, S.Y. (2012) In-situ
808 geochemistry of sulfides in highly metasomatized mantle xenoliths from Kerguelen, southern
809 Indian Ocean. Lithos, 154, 296–314. https://doi.org/10.1016/j.lithos.2012.07.018
810 Dobson, D.P., and Brodholt, J.P. (1999) The pressure medium as a solid-state oxygen
811 buffer. Geophysical Research Letters, 26(2), 259 – 262. https://doi.org/10.1029/1998GL900290
812 Evans, R.L., Jones, A.G., Garcia, X., Muller, M., Hamilton, M., Evans, S., Fourie, C.J.S.,
813 Spratt, J., Webb, S., Jelsma, H., Hutchins, D., (2011) Electrical lithosphere beneath the Kaapvaal
814 craton, southern Africa. Journal of Geophysical Research, 116(4), 1–16.
815 https://doi.org/10.1029/2010JB007883
816 Faul, U.H., Cline II, C.J., Berry, A., Jackson, I., and Garapić, G. (2018) Constraints on
817 oxygen fugacity within metal capsules. Physics and Chemistry of Minerals, 45, 497- 509.
818 https://doi.org/10.1007/s00269-017-0937-7
819 Fleet, M.E., and Stone, W.E. (1990) Nickeliferous sulfides in xenoliths, olivine
820 megacrysts, and basaltic glass. Contributions to Mineralogy and Petrology, 105, 629–636.
821 https://doi.org/10.1007/BF00306529
822 Fleig, J., Jamnik, J., Maier, J., and Ludvig, J. (1996) Inductive loops in impedance
823 spectroscopy caused by electrical shielding. Journal of the Electrochemical Society, 143 (11),
824 3636 – 3641. https://doi.org/10.1149/1.1837263
825 Fontboté, L., Kouzmanov, K., Chiaradia, M., and Pokrovski, G.S. (2017) Sulfide
826 minerals in hydrothermal deposits. Elements, 13(2), 97-103.
827 https://doi.org/10.2113/gselements.13.2.97
828 Fuller, B.D., and Ward, S.H. (1970) Linear system description of the electrical
829 parameters of rocks. IEEE Transactions on Geoscience Electronics, GE-8 (1). DOI:
830 10.1109/TGE.1970.271447
831 Gerhardt, R.A. (2005) Impedance spectroscopy and mobility spectra. In: Encyclopedia of
832 Condensed Matter Physics, Elsevier Press, 350-363.

Gibson, S.A., McMahon, S.C., Day, J.A., and Dawson, J.B. (2013) Highly refractory lithospheric mantle beneath the Tanzanian Craton: Evidence from Lashaine pre-metasomatic garnet-bearing peridotites. Journal of Petrology, 54 (8), 1503 – 1546. https://doi.org/10.1093/petrology/egt020

Glover, P.W.J. (2015) Geophysical properties of the near surface earth: Electrical properties. In: Schubert, G. (Ed) Treatise on Geophysics, 2nd edition, 11.04, pp 89 – 137. https://doi.org/10.1016/B978-0-444-53802-4.00189-5

Graf, J. L. and Skinner, B.J. (1970) Strength and deformation of pyrite and pyrrhotite. Economic Geology, 65 (2), 206 – 215. https://doi.org/10.2113/gsecongeo.65.2.206

Guo, J., Griffin, W.L., and O'Reilly, S.Y. (1999) Geochemistry and origin of sulphide minerals in mantle xenoliths: Qilin, southeastern China. Journal of Petrology, 40 (7), 1125–1149. https://doi.org/10.1093/petroj/40.7.1125

Hirsch, L.M., and Shankland, T.J. (1993) Quantitative olivine-defect chemical model: insights on electrical conduction, diffusion, and the role of Fe content. Geophysical Journal International, 114, 21-35. https://doi.org/10.1111/j.1365-246X.1993.tb01463.x

Huang, Y., Guo, H., Nakatani, T., Uesugi, K., Nakamura, M., and Keppler, H. (2021) Electrical conductivity in texturally equilibrated fluid-bearing forsterite aggregates at 800°C and 1 GPa: Implications for the high electrical conductivity anomalies in mantle wedges. Journal of Geophysical Research: Solid Earth, 126, e2020JB021343. https://doi.org/10.1029/2020JB021343

Huebner, J.S. and Dillenburg, R.G. (1995) Impedance of hot, dry silicate minerals and rock: Qualitative interpretation of spectra. American Mineralogist, 80 (1-2) , 46-64. https://doi.org/10.2138/am-1995-1-206

Jonscher, A.K. (1999) Dielectric relaxation in solids. Journal of Physics D: Applied Physics, 32 (14), R57. DOI 10.1088/0022-3727/32/14/201

Karato, S., Paterson, M.S., and FitzGerald, J.D. (1986) Rheology of synthetic olivine aggregates: Influence of grain size and water. Journal of Geophysical Research, 91, 8151-8176. https://doi.org/10.1029/JB091iB08p08151

Karato, S. (1989) Grain growth kinetics in olivine aggregates. Tectonophysics, 168 (4), 255 – 273. https://doi.org/10.1016/0040-1951(89)90221-7

Katsura, T., Yokoshi, S., Kawabe, K., Shatskiy, A., Okube, M., Fukui, H., Ito, E., Nozawa, A., and Funakoshi, K. (2007) Pressure dependence of electrical conductivity of $(Mg,Fe)SiO_3$ ilmenite. Physics and Chemistry of Minerals, 34, 249-255. https://doi.org/10.1007/s00269-007-0143-0

Kohlstedt, D.L. (2002) Partial melting and deformation. Chapter 5 of Plastic Deformation in Minerals and Rocks, eds. Karato, S., Wenk, H.-R., Reviews in Mineralogy and Geochemistry, Mineralogical Society of America, vol. 51, pp. 105-125. https://doi.org/10.1515/9781501509285-009

Maumus, J., Bagdassarov, N., and Schmeling, H. (2005) Electrical conductivity and partial melting of mafic rocks under pressure. Geochimica et Cosmochimica Acta, 69 (19), 4703-4718. https://doi.org/10.1016/j.gca.2005.05.010

Minarik, B. (2003) The core of planet formation, Nature, 422, 126 – 128. https://www.nature.com/articles/422126a

Manthilake, G., Mookherjee, M., Bolfan-Casanova, N., and Andrault, D. (2015) Electrical conductivity of lawsonite and dehydrating fluids at high pressures and temperatures. Geophysical Research Letters, 42 (18), 7398–7405. https://doi.org/10.1002/2015GL064804

Nelson, P.H. and Van Voorhis, G.D. (1983) Estimation of sulfide content from induced polarization data. Geophysics, 48(1), 62 - 75. https://doi.org/10.1190/1.1441408

Ni, H., Keppler, H., and Behrens, H. (2011) Electrical conductivity of hydrous basaltic melts: implications for partial melting in the upper mantle. Contributions to Mineralogy and Petrology, 162, 637 – 650. https://doi.org/10.1007/s00410-011-0617-4

Nichols, S.J., and Mackwell, S.J. (1991) Grain growth in porous olivine aggregates. Physics and Chemistry of Minerals, 18, 269-278. https://doi.org/10.1007/BF00202580

Olhoeft, G.R. (1989) Electrical properties of rocks, in: Physical Properties of Rocks and Minerals, Volume II, Y.S. Touloukian, W.R. Judd, and R.F.Roy, Eds, Hemisphere Publishing Corporation, Chapter 9, pp 257-329.

O'Neill, H.St.C. (1986) Mo-MoO_2 (MOM) oxygen buffer and the free energy of formation of MoO_2. American Mineralogist, 71, 1007 – 1010.

Parkhomenko, E.I. (1967) Electrical Properties of Rocks, translated and edited by Keller, G.V. Plenum Press, New York, pp. 88, 90,105, 269.

Pearce, C.I., Pattrick, R.A.D., and Vaughan, D.J. (2006) Electrical and Magnetic Properties of Sulfides. Reviews in Mineralogy and Geochemistry, 61, 127-180. https://doi.org/10.2138/rmg.2006.61.3

Poe, B.T., and Xu, Y. (1999) In situ complex impedance spectroscopy of mantle minerals measured at 20 GPa and 1400 °C. Phase Transitions, 68, 453 – 466. https://doi.org/10.1080/01411599908224527

Pommier, A. (2014) Interpretation of magnetotelluric results using laboratory measurements. Surveys in Geophysics, 35, 41-84. https://doi.org/10.1007/s10712-013-9226-2

Pommier A., Leinenweber, K., and Tasaka, M. (2015) Experimental investigation of the electrical behavior of olivine during partial melting under pressure and application to the lunar mantle. Earth and Planetary Science Letters, 425, 242-255. http://dx.doi.org/10.1016/j.epsl.2015.05.052

Pommier A., Leinenweber, K, Tran T. (2019) Mercury's thermal evolution controlled by an insulating liquid outermost core? Earth and Planetary Science Letters, 517, 125-134. https://doi.org/10.1016/j.epsl.2019.04.022

Rai, C.S., and Manghnani, M.H. (1978) Electrical conductivity of ultramafic rocks to 1820 kelvin. Physics of the Earth and Planetary Interiors, 17, 6 – 13. https://doi.org/10.1016/0031-9201(78)90004-3

Revil, A., Vaudelet, P., Su, Z., and Chen, R. (2022) Induced polarization as a tool to assess mineral deposits: A review. Minerals, 12, 571. https://doi.org/10.3390/min12050571

Roberts, J.J., and Tyburczy, J.A. (1991) Frequency dependent electrical properties of polycrystalline olivine compacts. Journal of Geophysical Research, 96, 16205-16222. https://doi.org/10.1029/91JB01574

Rogers, G.R. (1966) The search for disseminated sulfides (Introduction). Chapter IV of SEG Mining Geophysics Volume I, Case Histories, edited by Hansen, D.A., Heinrichs, W.E., Holmer, R.C., MacDougall, R.E., Rogers, G.R., Sumner, J.S., Ward, S.H. pp 265 – 272. https://doi.org/10.1190/1.9781560802709.ch4

Rose, L.A., and Brenan, J.M. (2001) Wetting properties of Fe-Ni-Co-Cu-O-S melts against olivine: Implications for sulfide melt mobility. Economic Geology, 96, 145 – 157.

Rubie, D.C., Karato, S., Yan, H., and O'Neill, H.St.C. (1993) Low differential stress and controlled chemical environment in multianvil high-pressure experiments. Physics and Chemistry of Minerals, 20, 315 – 322. https://doi.org/10.1007/BF00215102

Ryzhenko, B., and Kennedy, G.C. (1973) The effect of pressure on the eutectic in the system Fe-FeS. American Journal of Science, 273 (9), 803 – 810. https://doi.org/10.2475/ajs.273.9.803

Saxena, S., Pommier, A., and Tauber, M.J. (2021) Iron sulfides and anomalous electrical resistivity in cratonic environments. Journal of Geophysical Research: Solid Earth, 126 (9), e2021JB022297. https://doi.org/10.1029/2021JB022297

Schock, R.N., Duba, A.G., and Shankland, T.J. (1989) Electrical conduction in olivine. Journal of Geophysical Research, 94, 5829–5839. https://doi.org/10.1029/JB094iB05p05829

Selway, K. (2014) On the causes of electrical conductivity anomalies in tectonically stable lithosphere. Surveys in Geophysics, 35, 219 – 257. https://doi.org/10.1007/s10712-013-9235-1

Silber, R.E., Secco, R.A., and Yong, W. (2017) Constant electrical resistivity of Ni along the melting boundary up to 9 GPa. Journal of Geophysical Research: Solid Earth, 122 (7), 5064 – 5081. https://doi.org/10.1002/2017JB014259

Solferino, G.F.D., Golabek, G.J., Nimmo, F., Schmidt, M.W. (2015) Fast grain growth of olivine in liquid Fe–S and the formation of pallasites with rounded olivine grains. Geochimica et Cosmochimica Acta, 162, 259–275.

Solferino, G.F.D., Golabek, G.J. (2018) Olivine grain growth in partially molten Fe–Ni–S: A proxy for the genesis of pallasite meteorites. Earth and Planetary Science Letters, 504, 38–52.

Solferino, G.F.D., Thomson, P.-R., and Hier-Majumder, S. (2020) Pore network modeling of core forming melts in planetesimals. Frontiers in Earth Science, 8, 339. https://doi.org/10.3389/feart.2020.00339

Sun, W., Dai, L., Hu, H., Wang, M., Hu, Z., and Jing, C. (2022) Experimental research on electrical conductivity of the olivine-ilmenite system at high temperatures and high pressures. Frontiers in Earth Science, 10, 861003. https://doi.org/10.3389/feart.2022.861003

Sun, W., Jiang, J., Dai, L., Hu, H., Wang, M., Qi, Y., and Li, H. (2021) Electrical properties of dry polycrystalline olivine mixed with various chromite contents: Implications for the high conductivity anomalies in subduction zones. Geoscience Frontiers, 12 (5) 101178. https://doi.org/10.1016/j.gsf.2021.101178

Terasaki, H., Frost, D.J., Rubie, D.C., and Langenhorst, F. (2005) The effect of oxygen and sulphur on the dihedral angle between Fe-O-S melt and silicate minerals at high pressure: Implications for Martian core formation. Earth and Planetary Science Letters, 232, 379-392. https://doi.org/10.1016/j.epsl.2005.01.030

Terasaki, H., Frost, D.J., Rubie, D.C., and Langenhorst, F. (2008) Percolative core formation in planetesimals. Earth and Planetary Science Letters, 273, 132 – 137. https://doi.org/10.1016/j.epsl.2008.06.019

Thiel, S., and Heinson, G. (2013) Electrical conductors in Archean mantle—Result of plume interaction? Geophysical Research Letters, 40, 2947-2952. https://doi.org/10.1002/grl.50486

Usselman, T.M. (1975) Experimental approach to the state of the core: Part I. The liquidus relations of the Fe-rich portion of the Fe-Ni-S system from 30 – 100 kb. American Journal of Science, 275 (3), 278 – 290. https://doi.org/10.2475/ajs.275.3.278

Walte, N.P., Becker, J.K., Bons, P.D., Rubie, D.C., and Frost, D.J. (2007) Liquid-distribution and attainment of textural equilibrium in a partially-molten crystalline system with a high-dihedral-angle liquid phase. Earth and Planetary Science Letters, 262, 517 – 532. https://doi.org/10.1016/j.epsl.2007.08.003

Walte, N.P., Rubie, D.C., Bons, P.D., and Frost, D.J. (2011) Deformation of a crystalline aggregate with a small percentage of high-dihedral-angle liquid: Implications for core–mantle differentiation during planetary formation. Earth and Planetary Science Letters, 305, 124-134. https://doi.org/10.1016/j.epsl.2011.02.049

Wanamaker, B.J., and Duba, A.G. (1993) Electrical conductivity of San Carlos olivine along [100] under oxygen- and pyroxene-buffered conditions and implications for defect equilibria. Journal of Geophysical Research, 98, 489–500. https://doi.org/10.1029/92JB01584

Wanamaker, B.J. (1994) Point defect diffusivites in San Carlos olivine derived from reequilibration of electrical conductivity following changes in oxygen fugacity. Geophysical Research Letters, 21 (1), 21 – 24. https://doi.org/10.1029/93GL02790

Wang, K.L., O'Reilly, S.Y., Honda, M., Matsumoto, T., Griffin, W.L., Pearson, N.J., and Zhang, M. (2010) Co-rich sulfides in mantle peridotites from Penghu Islands, Taiwan: Footprints of Proterozoic mantle plumes under the Cathaysia Block. Journal of Asian Earth Sciences, 37 (3), 229–245. https://doi.org/10.1016/j.jseaes.2009.08.008

Watson, H.C, Roberts, J.J., and Tyburczy, J.A. (2010) Effect of conductive impurities on electrical conductivity of polycrystalline olivine. Geophysical Research Letters, 37, L02302. https://doi.org/10.1029/2009GL041566

Watson, H.C., and Roberts, J.J. (2011) Connectivity of core forming melts: Experimental constraints from electrical conductivity and X-ray tomography. Physics of the Earth and Planetary Interiors, 186, 172–182. https://doi.org/10.1016/j.pepi.2011.03.009

Xu, Y., Poe, B.T., Shankland, T.J., Rubie, D.C. (1998) Electrical conductivity of olivine, wadsleyite, and ringwoodite under upper-mantle conditions. Science, 280, 1415 – 1418. https://doi.org/10.1126/science.280.5368.1415

Yoshino, T. (2010) Laboratory electrical conductivity measurement of mantle minerals. Surveys in Geophysics, 31, 163-206. https://doi.org/10.1007/s10712-009-9084-0

Yoshino, T., Walter, M.J., and Katsura, T. (2003) Core formation in planetesimals triggered by permeable flow. Nature, 422, 154–157. https://doi.org/10.1038/nature01459

Yoshino, T., Walter, M.J., and Katsura, T. (2004) Connectivity of molten Fe alloy in peridotite based on in situ electrical conductivity measurements: Implications for core formation in terrestrial planets. Earth and Planetary Science Letters, 222, 625–643. https://doi.org/10.1016/j.epsl.2004.03.010

Yoshino, T., Matsuzaki, T., Yamashita, S., and Katsura, T. (2006) Hydrous olivine unable to account for conductivity anomaly at the top of the asthenosphere. Nature, 443, 973–976. https://doi.org/10.1038/nature05223

Yoshino, T., Shimojuku, A., Shan, S., Guo, X., Yamazaki, D., Ito, E., Higo, Y., and Funakoshi, K. (2012) Effect of temperature, pressure and iron content on the electrical

conductivity of olivine and its high-pressure polymorphs. Journal of Geophysical Research, 117, B08205. https://doi.org/10.1029/2011JB008774

Zhdanov, M.S., Burtman, V., Endo, M., and Lin, W. (2018) Complex resistivity of mineral rocks in the context of the generalized effective-medium theory of the induced polarisation effect. Geophysical Prospecting, 66, 798 – 817. https://doi.org/10.1111/1365-2478.12581

This is the peer-reviewed, final accepted version for American Mineralogist, published by the Mineralogical Society of America.
The published version is subject to change. Cite as Authors (Year) Title. American Mineralogist, in press.
DOI: https://doi.org/10.2138/am-2023-9054. http://www.minsocam.org/

1013 # Tables

1014

Table 1. Experimental conditions. P = 2 GPa.

Run #	Composition	Amount of sulfide		Sulfide composition				Initial dwell		Quench T (K)[#]
		Vol%	Wt%	At. %Fe	At. % S	At. % Ni	At. % O	Temperature (K)	Duration (hr)	
BB281*	FeS + dunite	3.4	5.0	50	50	0	0	1023	5.0	1624
BB289*	FeS + dunite	6.5	10	50	50	0	0	1023	5.0	1627
BB291*	FeS + dunite	18.2	25	50	50	0	0	1023	6.0	1620
BB292	FeS + dunite	3.4	5.0	50	50	0	0	1023	23.8	1599
BB303	FeS + dunite	3.4	5.0	50	50	0	0	1023	3.5	1023
BB304	FeS + dunite	3.4	5.0	50	50	0	0	1023	23.7	1023
BB305	FeS + dunite	3.4	5.0	50	50	0	0	1023	23.7	569
BB290*	Fe-S-Ni + dunite	3.0	5.0	50	40	10	0	1023	6.0	1622
BB299	Fe-S-Ni + dunite	3.4	5.8	50	40	10	0	1023	27.2	1572
BB294	Fe-S-Ni + dunite	3.4	5.8	40	40	20	0	1023	27.4	1588
BB295	Fe-S-Ni + dunite	6.5	11.4	40	40	20	0	1023	27.1	1618
BB280*	FeS	100	100	50	50	0	0	1023	4.1	1626
BB288*	Fe-S-Ni	100	100	50	40	10	0	1023	4.0	1602
BB283*	Dunite	0	0	-	-	-	-	1023	4.5	1647
BB293*	Dunite	0	0	-	-	-	-	1023	24.6	1572

*From Saxena et al. 2021.

[#]Quench temperature corresponds to the maximum temperature for all experiments except BB305 (T_{max} = 1023 K).

1015
1016
1017

Table 2. Electron microprobe analyses of metal-sulfide phase in retrieved samples (in wt.%).

Sample	Phase	Fe		S		Ni		O		Total
BB280	S-low (3)[a]	77.7	*(16)*[b]	17.1	*(13)*	0.02	*(0)*	1.73	*(2)*	96.6
	S-high (2)	64.6	*(8)*	29.8	*(10)*	0.01	*(1)*	3.84	*(4)*	98.2
BB281	sulfide (6)	62.4	*(41)*	32.1	*(5)*	1.25	*(7)*	1.79	*(99)*	97.6
BB288	S-low (2)	98.4	*(2)*	0.07	*(1)*	0.01	*(1)*	0.18	*(3)*	98.6
	S-high (2)	87.0	*(26)*	10.4	*(2)*	0.01	*(1)*	0.78	*(24)*	98.2
BB289	sulfide (4)	64.1	*(37)*	32.4	*(27)*	0.30	*(18)*	1.46	*(4)*	98.2
BB290	S-low (3)	96.2	*(18)*	0.0	*(2)*	0.67	*(27)*	0.32	*(14)*	97.2
	S-high (1)	60.8	-	28.4	-	4.59	-	3.03	-	96.9
BB291	S-low (1)	84.2	-	12.4	-	0.17	-	1.32	-	98.0
	S-high (4)	71.7	*(39)*	27.1	*(43)*	0.16	*(2)*	1.94	*(69)*	100.8
BB292	sulfide (4)	67.1	*(48)*	29.7	*(37)*	0.53	*(42)*	1.03	*(4)*	98.3
BB294	S-low (2)	39.0	*(104)*	17.1	*(3)*	38.7	*(107)*	0.55	*(32)*	95.3
	S-high (5)	40.2	*(65)*	29.2	*(28)*	25.9	*(91)*	0.47	*(25)*	95.8
BB295	S-low (1)	66.4	-	20.7	-	9.79	-	2.46	-	99.3
	S-high (7)	51.4	*(85)*	33.5	*(24)*	13.0	*(101)*	0.49	*(35)*	98.4
BB299	S-low (4)	97.5	*(10)*	0.02	*(1)*	0.30	*(28)*	0.34	*(1)*	98.1
	S-high (3)	71.8	*(20)*	22.5	*(25)*	0.51	*(20)*	1.49	*(30)*	96.4
BB303	sulfide (7)	60.9	*(12)*	37.4	*(9)*	0.07	*(2)*	0.40	*(33)*	98.9
BB304	sulfide (3)	62.4	*(57)*	33.7	*(66)*	0.07	*(4)*	1.57	*(12)*	97.7

a: Number of microprobe analyses.

1018 b: One standard deviation of replicate analyses in terms of least unit cited.

This is the peer-reviewed, final accepted version for American Mineralogist, published by the Mineralogical Society of America.
The published version is subject to change. Cite as Authors (Year) Title. American Mineralogist, in press.
DOI: https://doi.org/10.2138/am-2023-9054. http://www.minsocam.org/

Table 3. Electron microprobe analyses of silicates and oxides in retrieved samples (in wt.%).

Sample	Phase	SiO_2		TiO_2		Al_2O_3		Cr_2O_3		FeO		MnO		MgO		CaO		Na_2O		K_2O		NiO		P_2O_5		S		Total	Mg#[c]
Dunite starting powder oil (11)[a]		40.9	(4)[b]	0.02	(2)	0.02	(1)	0.04	(2)	13.6	(18)	0.18	(2)	45.9	(15)	0.10	(1)	0.01	(1)	0.00	(0)	0.33	(4)	0.01	(1)	-	-	101.0	85.7
BB281	ol (9)	39.7	(2)	0.07	(5)	0.10	(4)	0.05	(1)	14.3	(6)	0.19	(3)	45.3	(7)	0.25	(12)	0.01	(1)	0.00	(0)	0.22	(8)	0.10	(6)	0.00	(0)	100.3	84.9
	Near electrode ol (2)	38.1	(11)	0.06	(0)	0.11	(2)	0.06	(1)	22.5	(48)	0.15	(1)	38.6	(41)	0.14	(3)	0.00	(0)	0.00	(0)	0.21	(7)	0.31	(5)	0.02	(2)	100.3	75.2
BB289	ol (16)	39.0	(3)	0.06	(3)	0.21	(26)	0.04	(2)	14.1	(7)	0.19	(2)	44.8	(6)	0.29	(15)	0.01	(1)	0.04	(12)	0.17	(10)	0.06	(4)	0.04	(7)	98.9	85.0
	Near electrode ol (7)	36.9	(8)	0.06	(2)	0.14	(3)	0.05	(9)	23.9	(30)	0.64	(45)	36.5	(24)	0.31	(7)	0.01	(2)	0.00	(1)	0.04	(0)	0.24	(9)	0.02	(2)	98.9	73.1
	cpx (2)	50.0	(3)	0.78	(25)	3.39	(21)	0.86	(41)	5.21	(16)	0.09	(2)	18.0	(45)	19.7	(22)	0.57	(5)	0.01	(0)	-	-	0.03	(3)	0.01	(0)	98.6	85.7
BB290	ol (5)	39.8	(2)	0.06	(1)	0.13	(9)	0.05	(3)	15.2	(7)	0.18	(1)	44.5	(6)	0.25	(8)	0.02	(1)	0.01	(0)	-	-	0.03	(2)	0.00	(0)	100.2	83.9
	Near electrode ol (6)	38.9	(7)	0.15	(6)	0.81	(60)	0.09	(8)	17.0	(3)	0.20	(0)	42.9	(6)	0.37	(20)	0.02	(1)	0.01	(0)	-	-	0.19	(17)	0.01	(1)	100.7	81.8
	Near sulfide ol (8)	39.4	(2)	0.07	(1)	0.15	(3)	0.06	(2)	16.4	(2)	0.20	(0)	43.50	(4)	0.36	(9)	0.02	(1)	0.02	(3)	-	-	0.08	(5)	0.00	(0)	100.2	82.5
	cpx (1)	50.8	-	0.84	-	5.62	-	0.66	-	4.11	-	0.06	-	16.0	-	21.2	-	0.53	-	0.02	-	-	-	0.04	-	0.00	-	99.8	87.4
BB291	ol (24)	40.0	(4)	0.02	(2)	0.03	(1)	0.03	(2)	13.6	(7)	0.19	(3)	46.1	(8)	0.13	(7)	0.01	(1)	0.00	(0)	0.33	(4)	0.01	(1)	0.01	(0)	100.4	85.8
	Near sulfide ol (6)	38.6	(5)	0.03	(3)	0.23	(16)	0.03	(2)	18.8	(11)	0.20	(2)	41.5	(11)	0.65	(14)	0.03	(2)	0.01	(0)	0.07	(6)	0.08	(7)	0.07	(8)	100.3	79.7
BB292	ol (16)	40.0	(3)	0.06	(3)	0.07	(3)	0.04	(2)	14.1	(5)	0.19	(2)	45.6	(6)	0.17	(8)	0.00	(0)	0.00	(0)	-	-	0.08	(8)	0.04	(7)	100.3	85.3
	Near electrode ol (6)	38.3	(2)	0.06	(3)	0.14	(4)	0.01	(1)	20.7	(12)	0.23	(3)	40.2	(10)	0.14	(1)	0.00	(0)	0.00	(0)	-	-	0.21	(2)	0.06	(5)	100.1	77.5
	Near sulfide ol (1)	38.5	-	0.03	-	0.06	-	0.01	-	21.2	-	0.14	-	39.4	-	0.11	-	0.01	-	0.00	-	-	-	0.10	-	0.00	-	99.5	76.8
	cpx (4)	50.7	(7)	1.59	(1)	2.61	(3)	0.70	(38)	5.36	(6)	0.08	(1)	15.6	(6)	22.3	(3)	0.41	(8)	0.01	(0)	-	-	0.05	(6)	0.07	(8)	99.5	83.8
	opx (1)	54.9	-	0.16	-	1.60	-	0.25	-	12.2	-	0.15	-	29.7	-	0.92	-	0.03	-	0.00	-	-	-	0.02	-	0.22	-	100.2	81.2
BB293	ol (16)	40.1	(3)	0.08	(5)	0.10	(12)	0.04	(3)	13.8	(4)	0.19	(1)	45.2	(5)	0.13	(6)	0.01	(1)	0.00	(0)	-	-	0.12	(10)	0.00	(1)	99.8	85.4
	Near electrode ol (5)	39.6	(3)	0.03	(2)	0.07	(4)	0.03	(1)	16.5	(4)	0.16	(1)	43.3	(2)	0.08	(4)	0.02	(1)	0.00	(0)	-	-	0.17	(21)	0.00	(0)	100.0	82.4
	cpx (3)	52.5	(20)	1.37	(9)	2.65	(9)	0.60	(50)	5.24	(11)	0.09	(3)	15.8	(17)	21.1	(20)	0.65	(35)	0.01	(0)	-	-	0.02	(1)	0.00	(0)	100.0	84.2
BB295	ol (12)	40.3	(1)	0.02	(1)	0.03	(1)	0.03	(1)	13.1	(2)	0.17	(2)	46.3	(2)	0.11	(3)	0.01	(1)	0.00	(0)	0.43	(4)	0.01	(1)	0.00	(0)	100.5	86.3
	Near electrode ol (6)	39.1	(4)	0.06	(1)	0.13	(7)	0.03	(1)	18.9	(8)	0.25	(10)	41.4	(10)	0.20	(5)	0.00	(0)	0.00	(0)	0.21	(9)	0.13	(8)	0.04	(7)	100.5	79.6
	Near sulfide ol (10)	39.5	(2)	0.06	(3)	0.14	(6)	0.04	(2)	16.4	(4)	0.18	(1)	43.0	(4)	0.4	(9)	0.01	(1)	0.00	(0)	0.43	(11)	0.05	(5)	0.01	(1)	100.2	82.4
BB303	ol (24)	40.3	(3)	0.02	(2)	0.03	(2)	0.03	(2)	13.2	(5)	0.18	(2)	46.0	(6)	0.11	(3)	0.01	(1)	0.00	(1)	0.35	(2)	0.01	(2)	0.01	(1)	100.1	86.1
	Near sulfide ol (3)	39.0	(12)	0.05	(2)	0.09	(10)	0.03	(3)	16.1	(7)	0.20	(1)	43.7	(7)	0.18	(7)	0.03	(1)	0.01	(1)	0.31	(7)	0.06	(5)	0.24	(28)	100.0	82.8
	cpx (7)	53.4	(4)	0.88	(9)	1.55	(15)	1.04	(24)	4.10	(33)	0.08	(3)	16.5	(5)	22.0	(5)	0.46	(5)	0.00	(1)	0.05	(1)	0.00	(1)	0.00	(0)	100.0	87.7
BB304	ol (10)	40.2	(6)	0.03	(2)	0.04	(2)	0.04	(2)	13.4	(9)	0.18	(1)	46.1	(9)	0.12	(2)	0.01	(1)	0.00	(0)	-	-	0.03	(0)	0.02	(4)	100.2	85.9
	Near electrode ol (2)	38.9	(5)	0.07	(1)	0.09	(5)	0.05	(1)	19.4	(7)	0.17	(0)	41.8	(2)	0.12	(2)	0.00	(0)	0.01	(0)	-	-	0.06	(7)	0.01	(0)	100.6	79.3
	Near sulfide ol (1)	38.7	-	0.17	-	0.14	-	0.03	-	16.1	-	0.19	-	43.8	-	0.19	-	0.00	-	0.00	-	-	-	0.18	-	0.05	-	99.6	82.9
	cpx (4)	50.3	(17)	1.85	(9)	2.98	(9)	0.50	(56)	6.02	(14)	0.09	(2)	15.2	(15)	21.5	(9)	0.47	(8)	0.01	(2)	-	-	0.04	(0)	-	-	99.0	81.7

a: Number of microprobe analyses.
b: One standard deviation in terms of least unit cited.
c: Mg# = 100 x at. Mg/(Mg + Fe)

Table 4. Activation energies for DC conductivity (NA: not applicable).

Experiment	Composition	Low T		Intermediate T		High T	
		T range (K)	Ea (eV)	T range (K)	Ea (eV)	T range (K)	Ea (eV)
BB283	Dunite	672-1016	0.85 ± 0.01	1016-1251	1.70 ± 0.04	1251-1646	0.07 ± 0.02
BB293	Dunite	577-746	0.18 ± 0.03	1046-1172	1.62 ± 0.06	1172-1370	0.60 ± 0.04
		746-1046	0.56 ± 0.03				
BB281	3.4 vol.% FeS	573-773	0.14 ± 0.01	1051-1220	1.90 ± 0.08	1220-1495	0.31 ± 0.04
		773-1051	0.83 ± 0.03			1495-1624	3.50 ± 0.39
BB289	6.5 vol.% FeS	650-1028	0.16 ± 0.01	1028-1218	2.40 ± 0.20	1218-1326	0.83 ± 0.09
BB291	18.2 vol.% FeS	672-1025	0.04 ± 0.00	1025-1245	0.27 ± 0.02	1319-1447	0.12 ± 0.05
BB292	3.4 vol.% FeS	573-848	0.18 ± 0.01	1052-1195	1.65 ± 0.05	1245-1352	0.20 ± 0.07
		848-1052	0.50 ± 0.02				
BB305	3.4 vol.% FeS	569-851	0.25 ± 0.02	NA	NA	NA	NA
		851-1018	0.50 ± 0.02				
BB290	3.0 vol.% $Fe_{50}S_{40}Ni_{10}$	675-1051	0.87 ± 0.02	1051-1272	1.41 ± 0.05	1272-1447	0.48 ± 0.04
						1447-1622	0.91 ± 0.15
BB299	3.4 vol.% $Fe_{50}S_{40}Ni_{10}$	673-1098	1.13 ± 0.01	1098-1220	1.89 ± 0.03	1220-1446	0.85 ± 0.06
						1446-1572	1.93 ± 0.16
BB294	3.4 vol.% $Fe_{40}S_{40}Ni_{20}$	620-1040	0.47 ± 0.01	1040-1267	1.39 ± 0.03	1267-1446	0.25 ± 0.07
						1446-1549	1.93 ± 0.16
BB295	6.5 vol.% $Fe_{40}S_{40}Ni_{20}$	576-823	0.43 ± 0.02	1097-1248	1.47 ± 0.03	1248-1468	0.46 ± 0.04
		823-1097	0.89 ± 0.02			1468-1618	5.58 ± 0.71

This is the peer-reviewed, final accepted version for American Mineralogist, published by the Mineralogical Society of America.
The published version is subject to change. Cite as Authors (Year) Title. American Mineralogist, in press.
DOI: https://doi.org/10.2138/am-2023-9054. http://www.minsocam.org/

1024 **Figures and captions:**
1025

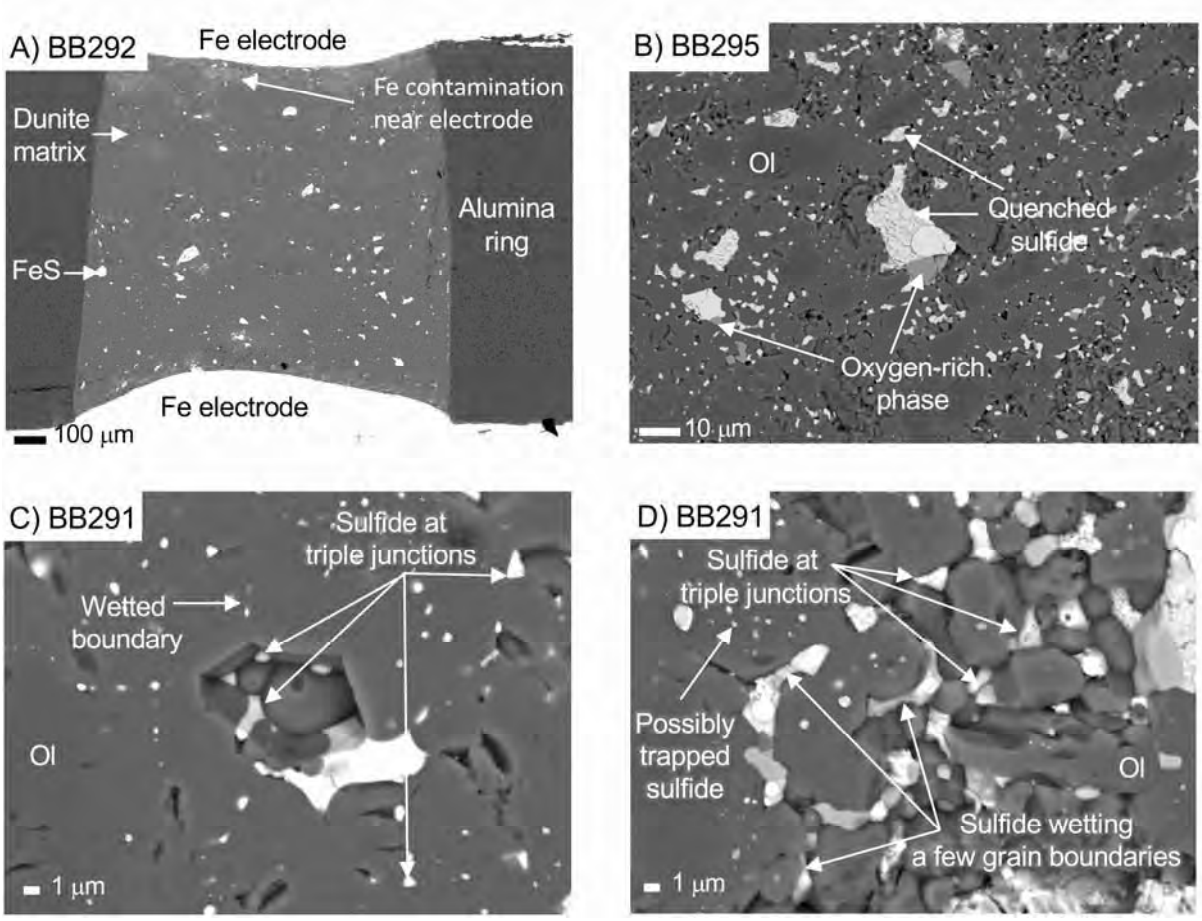

1026
1027
1028 **Figure 1**: Back-scattered electron (BSE) images from electron microprobe analyses on selected
1029 samples. A) Full cross section of quenched sample BB292 (3.4 vol.% FeS) with Fe electrodes
1030 visible at the top and bottom. B) Sulfide distribution in sample BB295 (6.5 vol.% Fe-S-Ni). C,
1031 D) Sulfide distribution in sample BB291 (18.2 vol.% FeS).
1032

This is the peer-reviewed, final accepted version for American Mineralogist, published by the Mineralogical Society of America.
The published version is subject to change. Cite as Authors (Year) Title. American Mineralogist, in press.
DOI: https://doi.org/10.2138/am-2023-9054. http://www.minsocam.org/

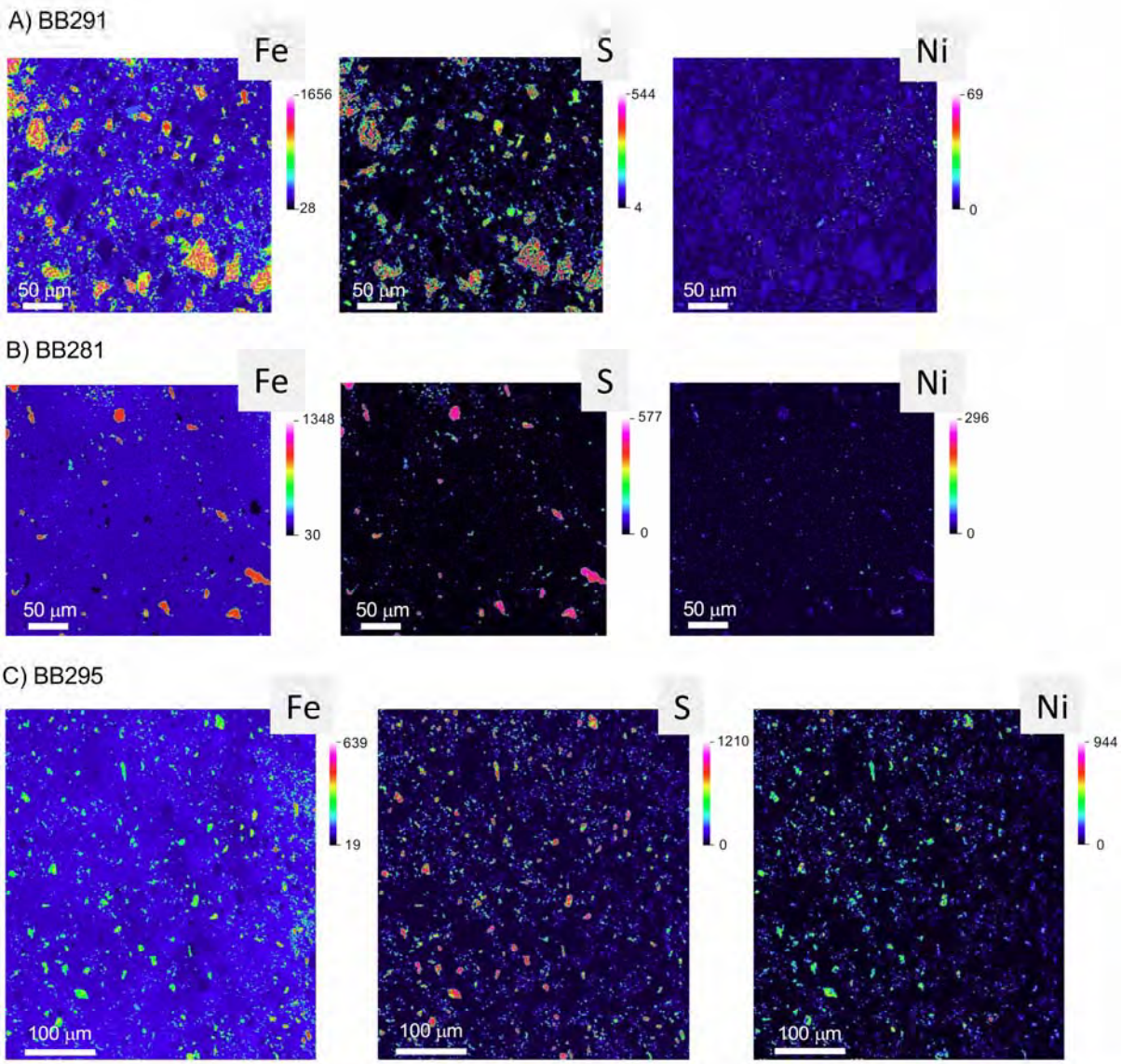

Figure 2: Wavelength dispersive spectroscopy (WDS) maps for elements Fe, S, and Ni, for selected samples. Numbers on the color scale indicate counts. (A) BB291, 18.2 vol.% FeS; (B) BB281, 3.4 vol.% FeS; (C) BB295, 6.5 vol.% Fe-S-Ni. The images in row C are larger to give a similar scale for this set, relative to rows A and B.

This is the peer-reviewed, final accepted version for American Mineralogist, published by the Mineralogical Society of America.
The published version is subject to change. Cite as Authors (Year) Title. American Mineralogist, in press.
DOI: https://doi.org/10.2138/am-2023-9054. http://www.minsocam.org/

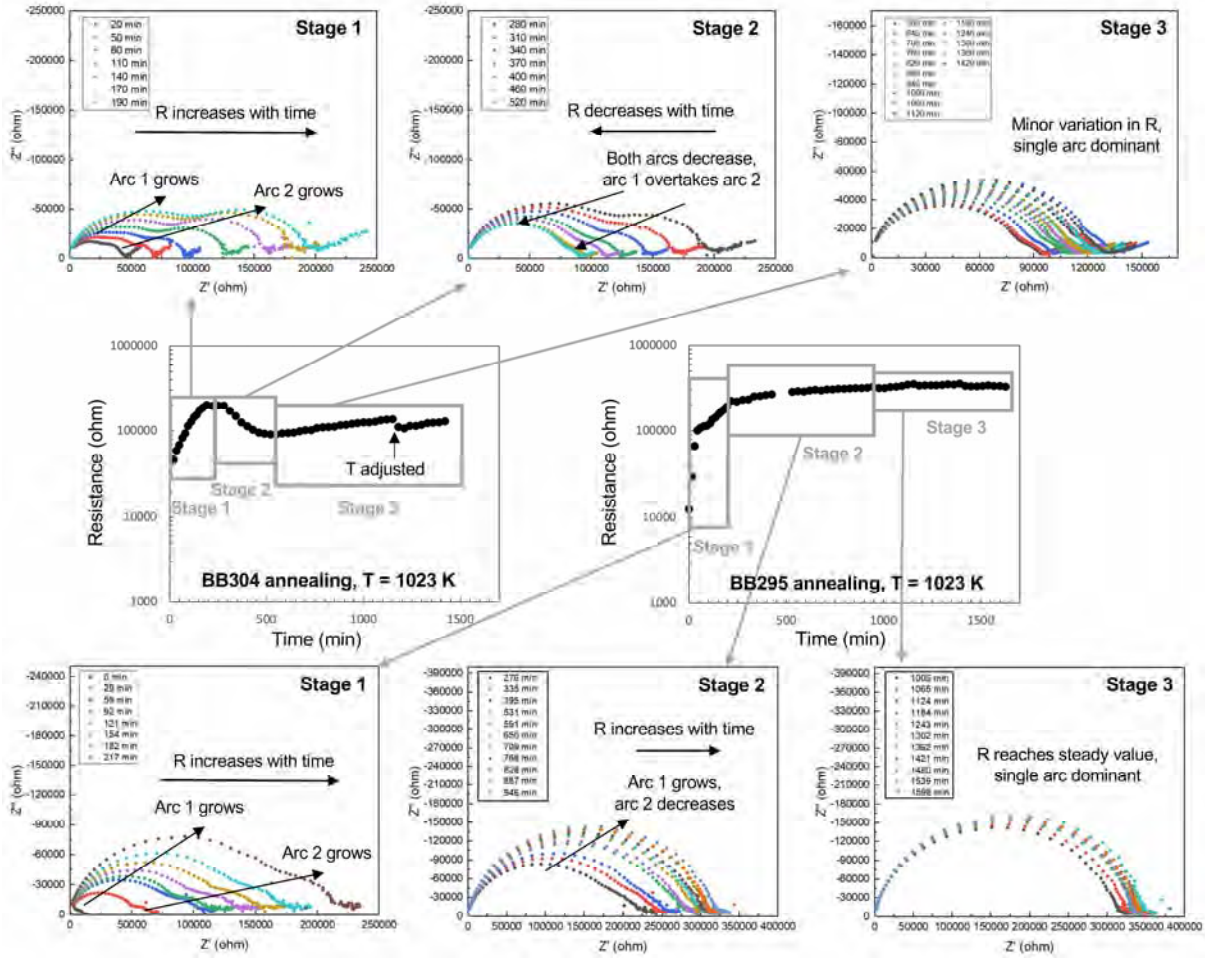

Figure 3: Changes in DC resistance and impedance spectra during annealing at 1023 K. Three stages can be identified (see text). Left-middle panel, and upper three panels: Sample BB304, 3.4 vol.% FeS in dunite; Right-middle panel, and three lower panels: Sample BB295, 6.5 vol.% Fe-S-Ni in dunite. The adjustment in T at ~1150 minutes for BB304 corrects a 20 K decline.

This is the peer-reviewed, final accepted version for American Mineralogist, published by the Mineralogical Society of America.
The published version is subject to change. Cite as Authors (Year) Title. American Mineralogist, in press.
DOI: https://doi.org/10.2138/am-2023-9054. http://www.minsocam.org/

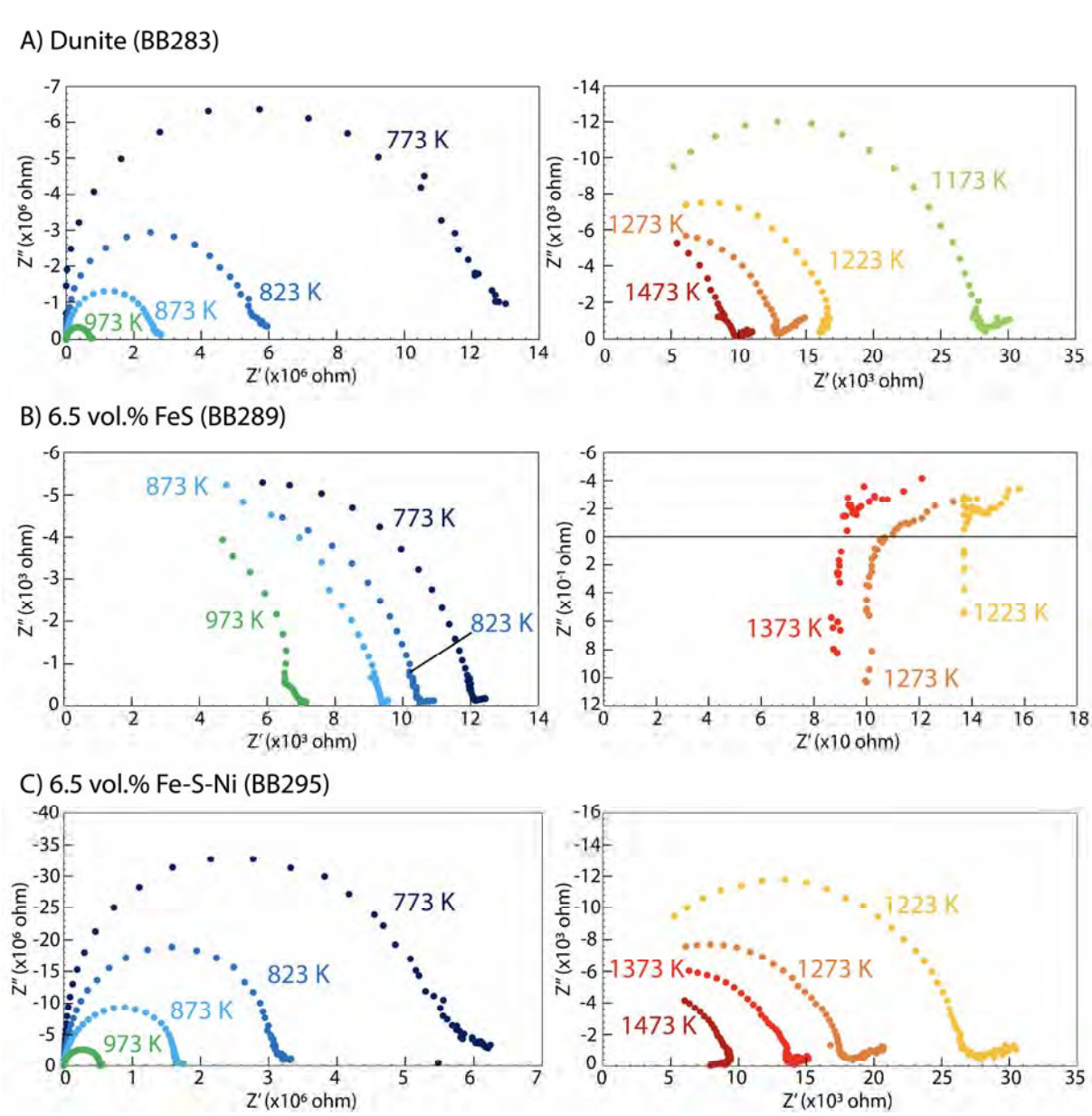

Figure 4: Impedance spectra at temperatures 673-1573 K for (A) Pure dunite (BB283), (B) 6.5 vol.% FeS (BB289), and (C) 6.5 vol.% $Fe_{40}S_{40}Ni_{20}$ (BB295).

This is the peer-reviewed, final accepted version for American Mineralogist, published by the Mineralogical Society of America.
The published version is subject to change. Cite as Authors (Year) Title. American Mineralogist, in press.
DOI: https://doi.org/10.2138/am-2023-9054. http://www.minsocam.org/

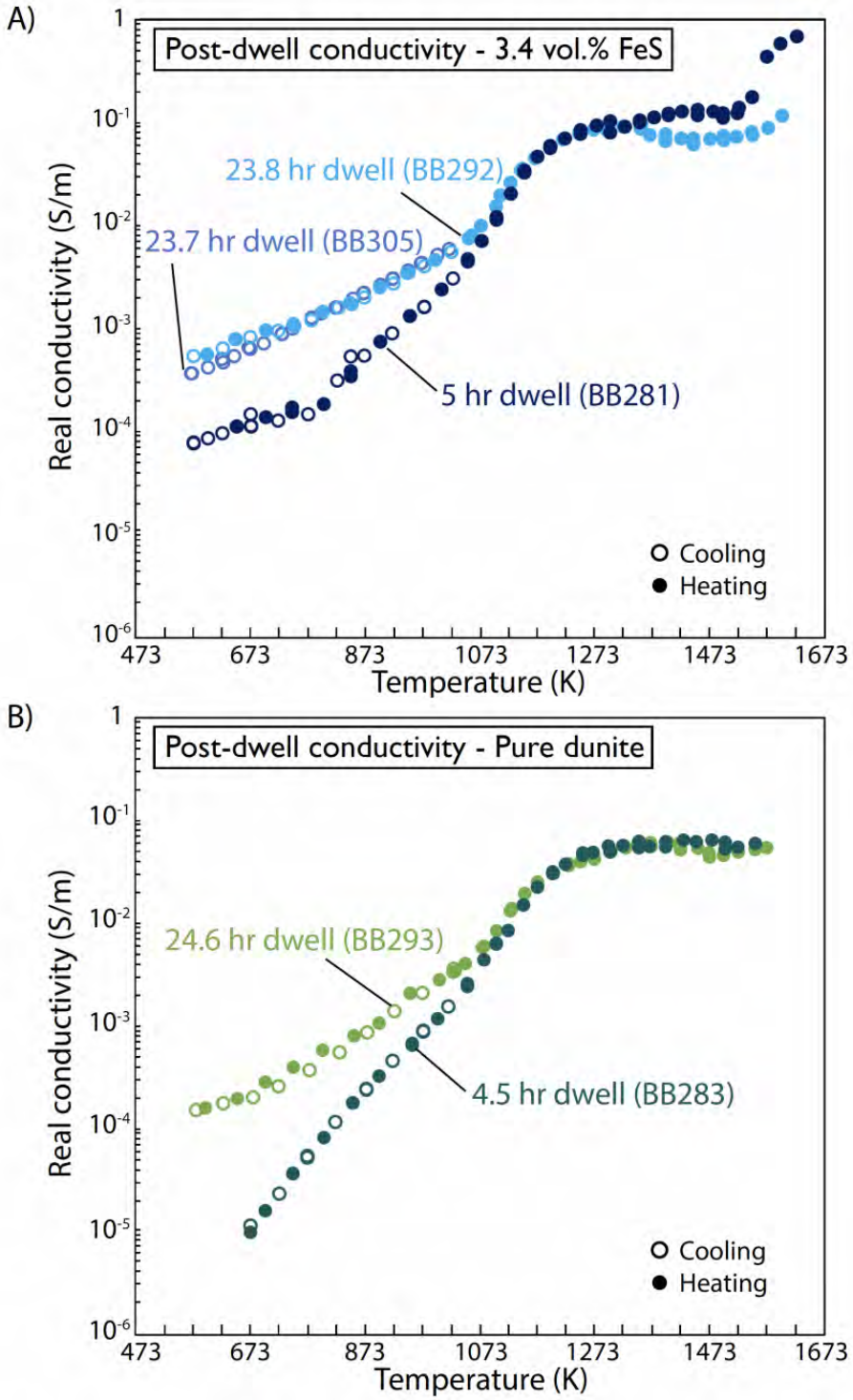

Figure 5: Effect of annealing (or dwell) duration on subsequent variable-temperature conductivity data for (A) samples with 3.4 vol. % FeS (BB281, BB292 and BB305), and (B) pure dunite samples BB283 and BB293. Open and filled circles correspond to measurements while cooling and heating, respectively.

This is the peer-reviewed, final accepted version for American Mineralogist, published by the Mineralogical Society of America.
The published version is subject to change. Cite as Authors (Year) Title. American Mineralogist, in press.
DOI: https://doi.org/10.2138/am-2023-9054. http://www.minsocam.org/

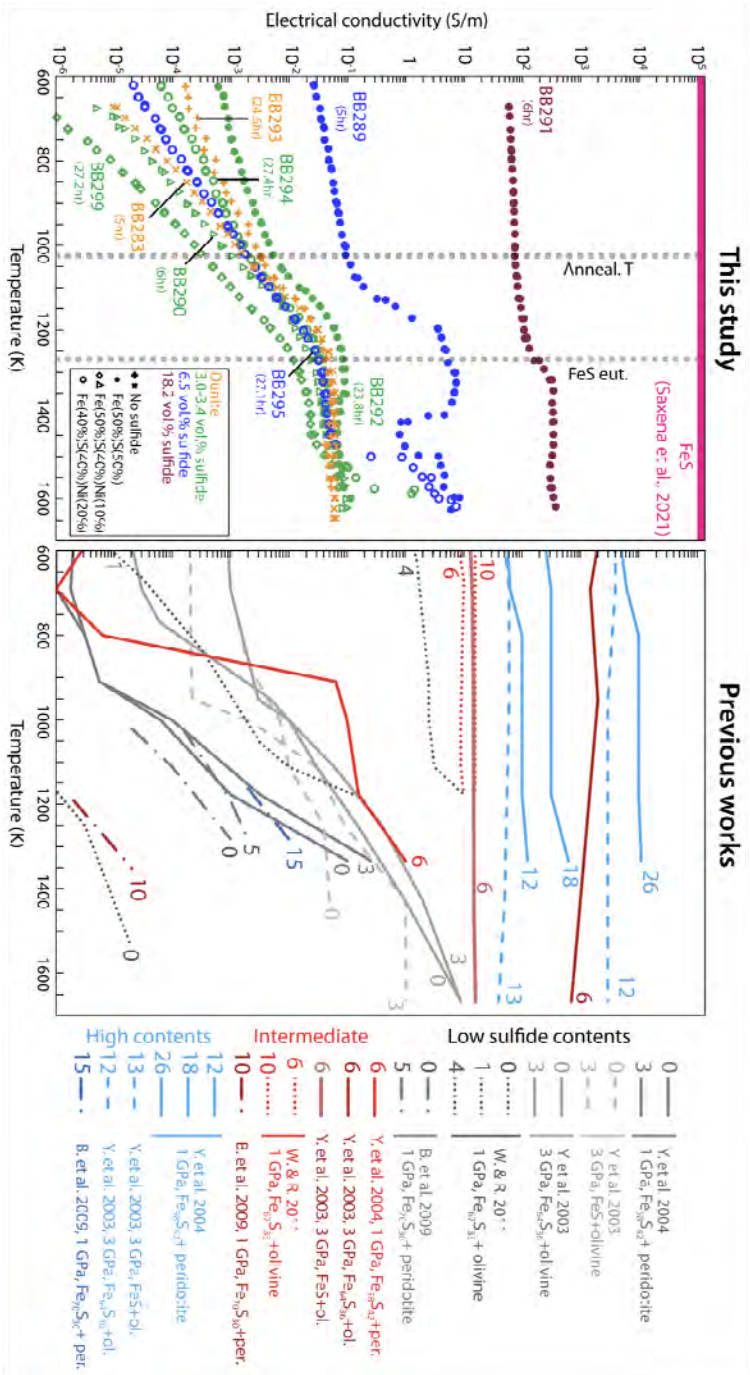

Figure 6: (Left panel) Conductivity extrapolated to 0 Hz (DC) vs. temperature for representative FeS or Fe-S-Ni/dunite mixtures, compared with pure FeS or dunite. Samples with 3.0 - 3.4, 6.5, 18.2 vol. % metal sulfide are in green, blue, and maroon, respectively. (Right panel) Conductivity trends from previous studies by Yoshino et al. (2003, 2004) (Y. et al.), Bagdassarov et al. (2009a) (B. et al.), and Watson and Roberts (2011) (W&R). The trendlines for W&R are corrected from Saxena et al. (2021). The data for B. et al. represent the conductivities as reached at the last stage of each experiment.

This is the peer-reviewed, final accepted version for American Mineralogist, published by the Mineralogical Society of America.
The published version is subject to change. Cite as Authors (Year) Title. American Mineralogist, in press.
DOI: https://doi.org/10.2138/am-2023-9054. http://www.minsocam.org/

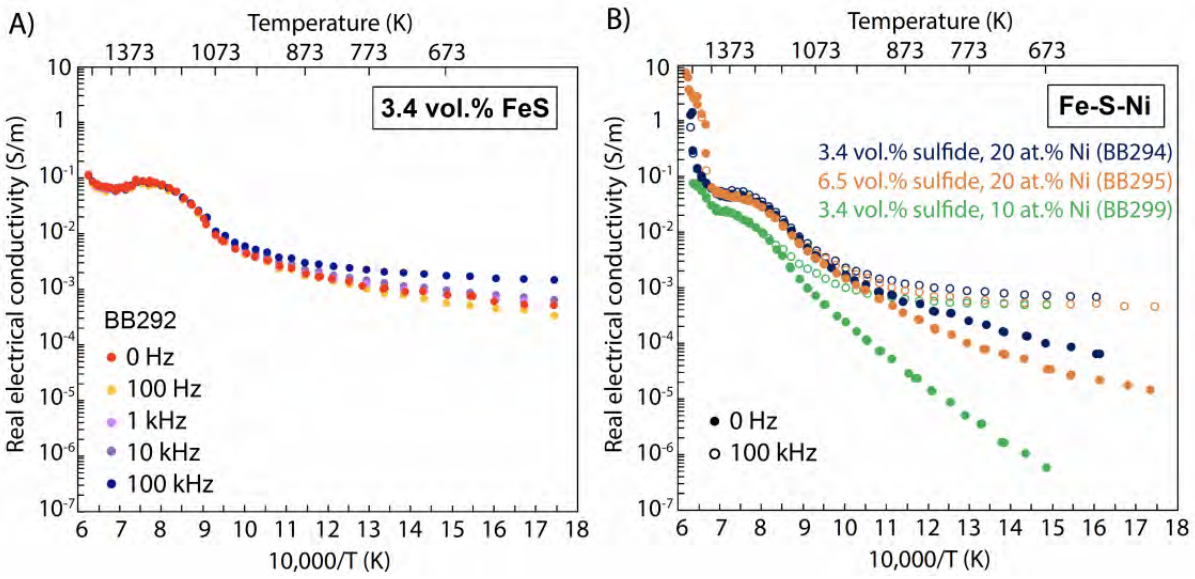

Figure 7: Real conductivity as a function of inverse T and frequency for experiments. A) BB292 (3.4 vol. % FeS). B) Fe-S-Ni samples (BB294, 295, and 299). The values at 0 Hz (DC) are extrapolated; the values for frequencies 100 Hz – 100 kHz are determined from Eq. 2 (see text).